

Physics-based machine learning for modeling stochastic IP3-dependent calcium dynamics

Oliver K. Ernst,^{1,2} Tom Bartol,² Terrence Sejnowski,^{2,3} and Eric Mjolsness⁴

¹*Department of Physics, University of California at San Diego, La Jolla, California*

²*Salk Institute for Biological Studies, La Jolla, California*

³*Division of Biological Sciences, University of California at San Diego, La Jolla, California*

⁴*Departments of Computer Science and Mathematics,
and Institute for Genomics and Bioinformatics, University of California at Irvine, Irvine, California*

(Dated: September 14, 2021)

We present a machine learning method for model reduction which incorporates domain-specific physics through candidate functions. Our method estimates an effective probability distribution and differential equation model from stochastic simulations of a reaction network. The close connection between reduced and fine scale descriptions allows approximations derived from the master equation to be introduced into the learning problem. This representation is shown to improve generalization and allows a large reduction in network size for a classic model of inositol trisphosphate (IP3) dependent calcium oscillations in non-excitable cells.

I. INTRODUCTION

Modeling physical systems with machine learning is a growing research topic. Machine learning offers inference methods that can be computationally more efficient than first principles approaches, and that can generalize well from high dimensional datasets. Their successes in science span protein structure prediction [30] to solutions to the quantum many-body problem [7].

A key challenge is how to incorporate prior knowledge into the learning problem [2, 8, 25]. This includes physical laws, symmetries and conservation laws. For example, kernel methods have been improved by encoding symmetries [10], and convolutional neural networks (CNNs) have benefited from pose estimation [5]. However, it remains difficult to introduce domain knowledge such as physical laws into machine learning. Often, methods are used in a domain agnostic way [16, 17, 27, 29], in that physical processes are not introduced explicitly, but rather only implicitly present in the training data. For some applications this is an advantage [21, 23], but for scientific modeling it has at least three deficits. First, models can be challenging to train, having to internally rediscover already known function forms from large amounts of training data. Second, models can be difficult to interpret, requiring a large number of parameters to explain behavior that from first principles may be low dimensional. Third, the trained models may generalize poorly compared to approaches incorporating physical principles.

This paper introduces a method for modeling stochastic reaction networks that incorporates knowledge from the chemical master equation (CME) into the inference problem. This is made possible by representing the right hand side of a differential equation by a neural network [12, 13, 18, 22, 28, 31]. By using analytically derived approximations as inputs, the network is shown to improve generalization for a classic model of IP₃ dependent calcium oscillations [9]. Additionally, reaction network conservation laws are incorporated into the framework. From a subset of stochastic simulations, the trained model completes the full range of oscillations, and outperforms an equivalent domain-agnostic model. The proposed approach is one avenue to improve machine learning for scientific modelling with domain-specific knowledge.

A. Chemical kinetics at the fine scale

Consider a system described by the number of particles $\mathbf{n} = \{n_A, n_B, \dots\}$ of species $\{A, B, \dots\}$. The time evolution of the probability distribution over states $p(\mathbf{n}, t)$ is described by the CME:

$$\frac{dp(\mathbf{n}, t)}{dt} = \sum_{r=1}^R \sum_{\mathbf{n}'} [T_r(\mathbf{n}|\mathbf{n}')p(\mathbf{n}', t) - T_r(\mathbf{n}'|\mathbf{n})p(\mathbf{n}, t)], \quad (1)$$

where $T_r(\mathbf{n}|\mathbf{n}')$ is the propensity for the transition \mathbf{n}' to \mathbf{n} under a reaction indexed by r .

Only the simplest reaction networks are solvable exactly or perturbatively in the Doi-Peliti operator formalism [24]. Further, the differential equations for moments derived from (1) generally do not close - equations for lower order

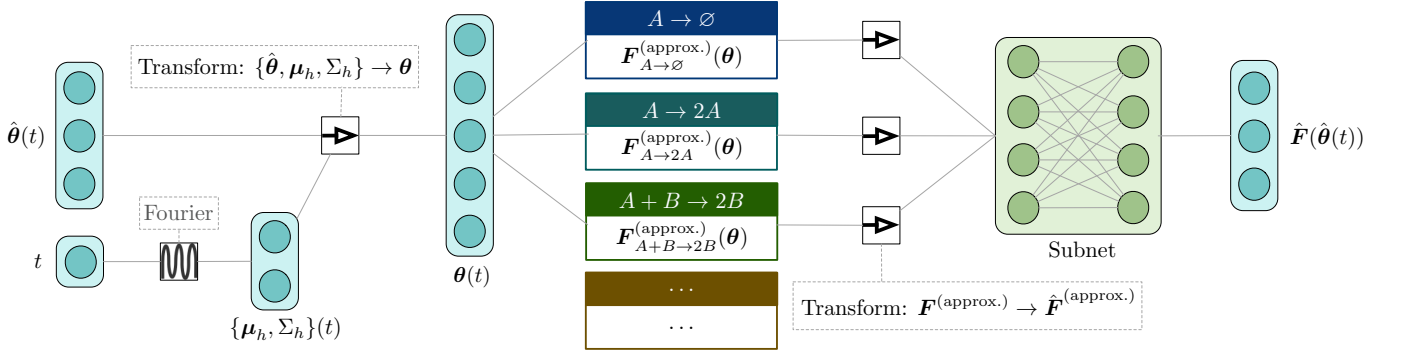


FIG. 1. Architecture for the differential equation model (11), where the right hand side is parameterized by a neural network. Inputs and outputs of the subnet are also standardized.

moments depend on higher orders. For example, for $A + B \rightarrow 2B$:

$$\begin{aligned} \frac{d\langle n_A \rangle}{dt} &\propto -\langle n_A n_B \rangle, \\ \frac{d\langle n_A n_B \rangle}{dt} &\propto -\langle n_A n_B^2 \rangle + \langle n_A^2 n_B \rangle - \langle n_A n_B \rangle. \end{aligned} \quad (2)$$

This infinite hierarchy requires a moment closure approximation, such as the Gaussian closure approximation:

$$p(\mathbf{n}, t) \sim \mathcal{N}(\mathbf{n} | \boldsymbol{\mu}_p(t), \Sigma_p(t)), \quad (3)$$

where $\boldsymbol{\mu}_p, \Sigma_p$ are the mean and covariance under p at an instant in time. In practice, it is challenging to choose the optimal closure approximation, since it is not clear which higher order moments will become relevant over long times.

Alternatively, the Gillespie algorithm [15] can be used to simulate stochastic trajectories of reaction networks. This is popular in biology [3, 19], at the cost of computation time for collecting sufficient statistics. Motivated by data-driven methods, we next propose a framework to learn closure approximations from stochastic simulations.

II. PHYSICS-BASED MACHINE LEARNING

A. Reduced model

We seek a reduced model that can be trained on stochastic simulations, but also incorporates physical knowledge to improve generalization. This connection can be made by a dynamic Boltzmann distribution (DBD) [12–14], consisting of an effective probability distribution with time-dependent interactions $\boldsymbol{\theta}(t)$ in the energy function:

$$\tilde{p}(\mathbf{n}; \boldsymbol{\theta}(t)) = \frac{1}{Z(t)} \exp[-E(\mathbf{n}; \boldsymbol{\theta}(t))], \quad (4)$$

and a differential equation system for the parameters:

$$\frac{d\boldsymbol{\theta}(t)}{dt} = \mathbf{F}(\boldsymbol{\theta}(t); \mathbf{u}), \quad (5)$$

for some functions \mathbf{F} with parameters \mathbf{u} , with a given initial condition $\boldsymbol{\theta}(t=0) = \boldsymbol{\theta}_0$. The Boltzmann distribution *ansatz* is motivated by the connection to graphical models [18]. In this work, the reduced model (4) considered is that of probabilistic principal component analysis (PCA), a popular choice for dimensionality reduction [4]. The parameters in the energy function are:

$$\boldsymbol{\theta}(t) = \{\mathbf{b}, W, \sigma^2, \boldsymbol{\mu}_h, \Sigma_h\}(t), \quad (6)$$

and the distribution is Gaussian:

$$\begin{aligned} \tilde{p}(\mathbf{n}; \boldsymbol{\theta}(t)) &= \mathcal{N}(\mathbf{n} | \boldsymbol{\mu}(t), C(t)), \\ \boldsymbol{\mu}(t) &= \begin{pmatrix} \mathbf{b} + W\boldsymbol{\mu}_h \\ \boldsymbol{\mu}_h \end{pmatrix} (t), \\ C(t) &= \begin{pmatrix} WW^\top + \sigma^2 I & W\Sigma_h \\ \Sigma_h W^\top & \Sigma_h \end{pmatrix} (t). \end{aligned} \quad (7)$$

Splitting the species into visible \mathbf{n}_v of size N_v and hidden \mathbf{n}_h of size N_h gives the more familiar form:

$$\begin{aligned}\tilde{p}(\mathbf{n}_h; \boldsymbol{\theta}(t)) &= \mathcal{N}(\mathbf{n}_h | \boldsymbol{\mu}_h, \Sigma_h), \\ \tilde{p}(\mathbf{n}_v | \mathbf{n}_h; \boldsymbol{\theta}(t)) &= \mathcal{N}(\mathbf{n}_v | \mathbf{b} + W(\boldsymbol{\mu}_h + \mathbf{n}_h), \sigma^2 I).\end{aligned}\quad (8)$$

B. Maximum likelihood at an instant in time

At an instant in time, $\boldsymbol{\mu}_h$ and Σ_h are arbitrary; across time, the differential equation (5) depends on these variables. For $\boldsymbol{\mu}_h = \mathbf{0}$ and $\Sigma_h = I$, the maximum likelihood (ML) solution is:

$$\begin{aligned}\hat{W}_{\text{ML}}(t) &= U_q(t)(L_q(t) - \sigma_{\text{ML}}^2(t)I)^{1/2}R, \\ \sigma_{\text{ML}}^2(t) &= \frac{1}{N_v - q} \sum_{i=q+1}^{N_v} \lambda_i(t), \\ \hat{\mathbf{b}}_{\text{ML}}(t) &= \frac{1}{M} \sum_{i=1}^M X_i(t),\end{aligned}\quad (9)$$

where M is the number of samples, $X(t)$ is the data matrix of size $M \times N_v$, and $U_q(t)$ and $L_q(t)$ are the normalized eigenvectors and eigenvalues of the data covariance matrix for the $1 \leq q \leq N_v$ largest eigenvalues. R is a rotation matrix that can be taken as $R = I$. The transformation to arbitrary $\boldsymbol{\mu}_h, \Sigma_h$ is:

$$\begin{aligned}\mathbf{b}_{\text{ML}}(t) &= \hat{\mathbf{b}}_{\text{ML}}(t) - \hat{W}_{\text{ML}}(t)\Sigma_h^{-1/2}(t)\boldsymbol{\mu}_h(t), \\ W_{\text{ML}}(t) &= \hat{W}_{\text{ML}}(t)\Sigma_h^{-1/2}(t).\end{aligned}\quad (10)$$

with matrix square root as $(A^{1/2})^\top A^{1/2} = A$. For convenience, let $\hat{\boldsymbol{\theta}}(t) = \{\hat{\mathbf{b}}, \hat{W}, \sigma^2\}(t)$ denote the *standard parameters*.

C. Linking snapshots in time

Given a set of training data, the ML parameters $\boldsymbol{\theta}_{\text{ML}}(t)$ can be obtained at each timepoint. To link snapshots in time, the form of the differential equations (5) must be chosen. The known CME physics is used to guide this choice by deriving an approximation $\mathbf{F}^{(\text{approx.})}$ to the true time evolution \mathbf{F} as follows.

At any point in time, the distribution defined by $\boldsymbol{\theta}(t)$ has observables $\boldsymbol{\phi}(t) = \{\boldsymbol{\mu}, C\}(t)$. For a single reaction like $A+B \rightarrow 2B$, these evolve as $d\boldsymbol{\phi}_{A+B \rightarrow 2B}/dt$ according to a hierarchy of moments like (2), derived from the CME. Under the Gaussian closure approximation (3), the equations for the moments are closed $d\boldsymbol{\phi}_{A+B \rightarrow 2B}/dt \sim d\boldsymbol{\phi}_{A+B \rightarrow 2B}^{(\text{closed})}/dt$. To convert back to the parameter frame, only some observables are tracked exactly. While arbitrary, the natural choice is $d\{\boldsymbol{\mu}_v, C_{vh}, \text{Tr}(C_v), \boldsymbol{\mu}_h, \Sigma_h\}/dt$ which match the dimensions of $\boldsymbol{\theta}$. The equations corresponding to this conversion $d\boldsymbol{\phi}_{A+B \rightarrow 2B}^{(\text{closed})}/dt \rightarrow d\boldsymbol{\theta}_{A+B \rightarrow 2B}^{(\text{closed})}/dt$ are obtained by differentiating (7). The result $\mathbf{F}_{A+B \rightarrow 2B}^{(\text{approx.})} \equiv d\boldsymbol{\theta}_{A+B \rightarrow 2B}^{(\text{closed})}/dt$ is an approximation to the time evolution of $\boldsymbol{\theta}(t)$ under this reaction (Supplemental material).

By considering a variety of reaction processes in this manner, a set of candidates was generated and used to parameterize the differential equations (5). It has been shown that the linearity of the CME in reactions extends to this form of the reduced model [12]. However, a linear model for (5) generalizes poorly when the data is not well-represented by a sparse set of available candidates [6].

Instead, let the right hand side of the differential equations (5) be given by a neural network with a special architecture shown in Figure 1. At each point in time with standard parameters $\hat{\boldsymbol{\theta}}(t)$, the inputs are the different reaction approximations. The outputs are the derivatives:

$$\frac{d\hat{\boldsymbol{\theta}}(t)}{dt} = \hat{\mathbf{F}}(\hat{\boldsymbol{\theta}}(t); \mathbf{u}), \quad (11)$$

where the parameters \mathbf{u} are those of the neural network. The model is trained to optimize the L_2 loss:

$$S = \sum_{t=1}^T \left(\frac{d\hat{\boldsymbol{\theta}}_{\text{ML}}(t)}{dt} - \hat{\mathbf{F}}(\hat{\boldsymbol{\theta}}_{\text{ML}}(t); \mathbf{u}) \right)^2. \quad (12)$$

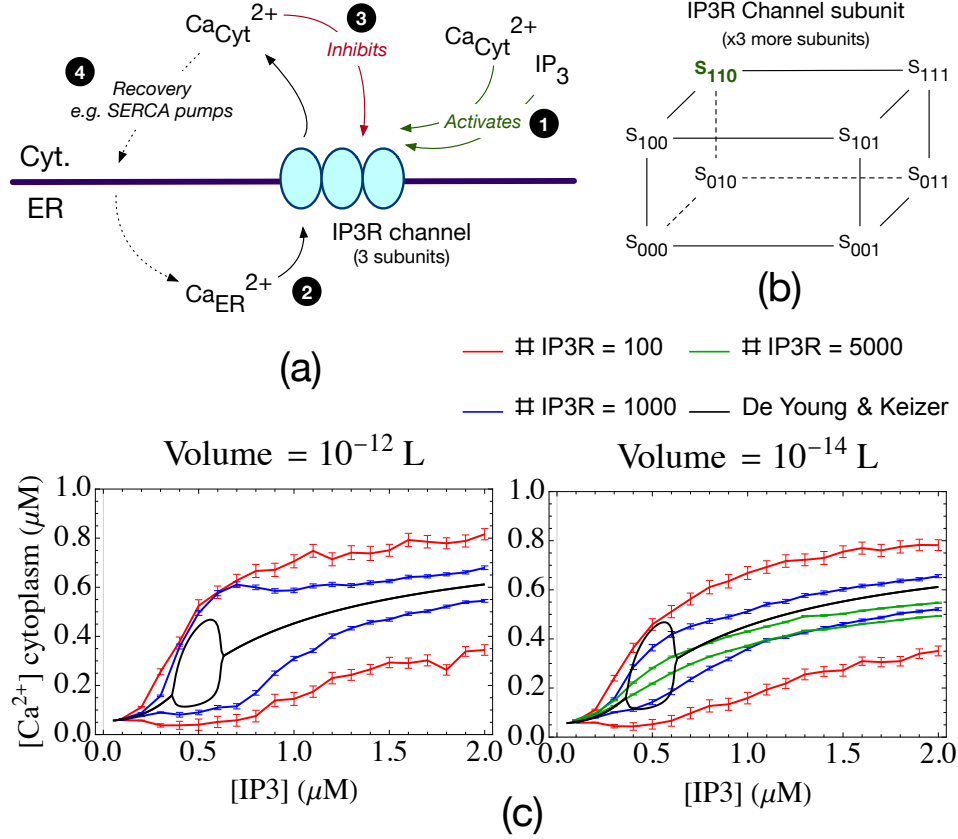


FIG. 2. (a) Schematic of IP₃ dependent calcium oscillations. Clusters of IP₃Rs in the ER membrane are activated by cytosolic calcium and IP₃ (1), allowing calcium transport into the cytoplasm (2). Further binding inhibits the channel (3), and eventual recovery recycles the calcium store (4). (b) Channel states of one of three subunits (Supplemental material). (c) Range of oscillations in the stochastic and deterministic [9] models for different volumes and numbers of IP₃Rs. Error bars indicate 95% confidence levels.

The training data is obtained from the ML parameters $\hat{\theta}_{\text{ML}}(t)$ for $t = 1, \dots, T$ by first computing $d\hat{\theta}_{\text{ML}}(t)/dt$ using total variation regularization [33] to differentiate the noisy signals. After training, the integration of (11) is stable if the Jacobian of the candidates $\partial \hat{\mathbf{F}}_{A+B \rightarrow 2B}^{(\text{approx.})} / \partial \hat{\theta}$ is small. To reduce the Jacobian, the data matrices $X(t)$ are transformed using a standardizing transformation (Supplemental material).

In principle, the standard parameters $\hat{\theta}$ where $\mu_h = \mathbf{0}$, $\Sigma_h = I$ can be used to calculate the reaction approximations. Instead, to improve generalization, the latent parameters μ_h, Σ_h are learned as a Fourier series. For a fixed set of L frequencies \mathbf{f} , let Σ_h be diagonal and let:

$$\begin{aligned}
 \mu_{h,i}(t) &= s(\mathbf{a}^{(\mu,i)}, \mathbf{b}^{(\mu,i)}), \\
 \Sigma_{h,i,i}(t) &= 1 + \epsilon + s(\mathbf{a}^{(\Sigma,i,i)}, \mathbf{b}^{(\Sigma,i,i)}), \\
 s(\mathbf{a}, \mathbf{b}) &= \frac{\sum_{l=1}^L (a_l \cos(f_l t) + b_l \sin(f_l t))}{\max\left(\sum_{l=1}^L (|a_l| + |b_l|), 1\right) + \epsilon},
 \end{aligned} \tag{13}$$

where ϵ is small and coefficients \mathbf{a}, \mathbf{b} are learned. This lets μ_h oscillate in $[-1, 1]$ and Σ_h around the identity. Finally, since μ_h, Σ_h are unknown from the data, the approximations $\mathbf{F}_{\text{reaction}}^{(\text{approx.})}$ are converted back to the standard space $\hat{\mathbf{F}}_{\text{reaction}}^{(\text{approx.})}$ using (10).

III. IP₃ DEPENDENT CALCIUM OSCILLATIONS

The proposed physics-based ML method is demonstrated for calcium oscillations in non-excitabile cells [32]. These occur due to calcium influx into the cytoplasm from stores in the endoplasmic reticulum (ER) through IP₃ receptors (IP₃R) in the membrane. A classic model by De Young and Keizer [9] uses ordinary differential equations and treats the channel at equilibrium, as shown in Figures 2.

A key result is a bifurcation diagram for calcium oscillations, shown in Figure 2(c). A Hopf bifurcation occurs at [IP₃] $\sim 0.4\mu\text{M}$ beyond which oscillations arise. Beyond [IP₃] $\sim 0.6\mu\text{M}$, a stable elevated level of calcium is observed.

Figure 2(c) compares the bifurcation diagram with the range of oscillations observed in a stochastic version of the De Young and Keizer [9] model. The receptor channel states and transport through the channel are simulated using the Gillespie method, with identical parameters to those in [9]. For the stochastic model, two cytoplasm volumes are considered: 10^{-12} L and 10^{-14} L, and the number of IP₃R is varied. The range of oscillations show the maximum/minimum over 40 s of the mean calcium concentration plus/minus a standard deviation. Spontaneous calcium spikes continue to arise in the stochastic model even at high IP₃ concentrations.

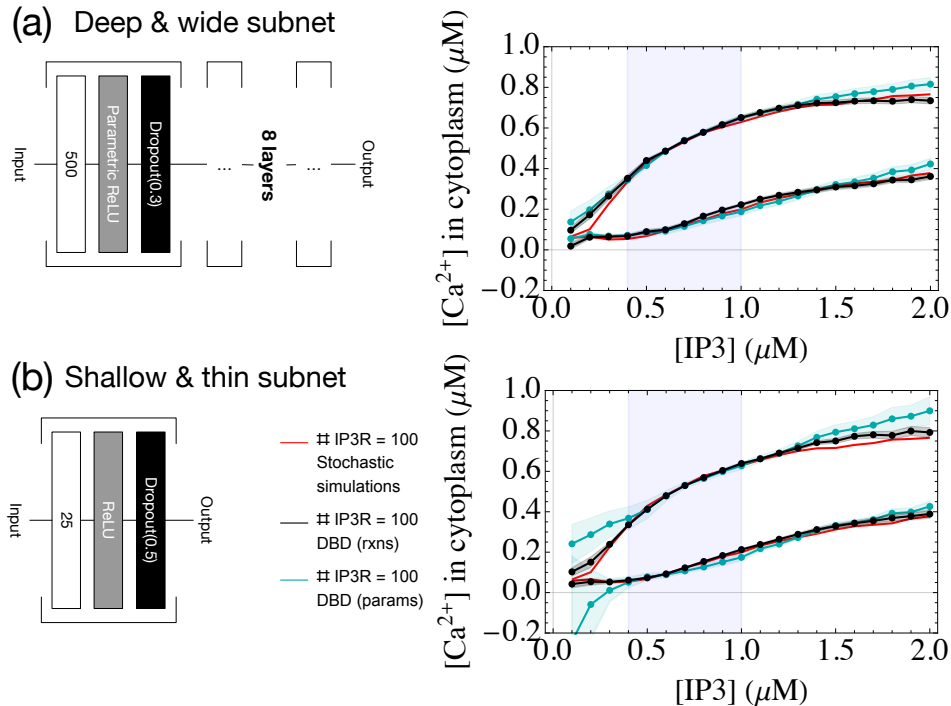


FIG. 3. Incorporating reaction approximations improves generalization (black). Two subnets are compared: (a) a deep & wide subnet, and (b) a shallow & thin subnet. The IP₃ concentrations used as training data are highlighted (blue). A comparison architecture using the same subnet but missing reaction approximations is also shown (cyan). Shading shows 95% confidence intervals from 10 optimization trials.

A. Learning calcium oscillations

The DBD architecture is applied to learn calcium oscillations over a subset of IP₃ concentrations (all code is available online [11]). Figure 3 shows the range of oscillations learned for $V = 10^{-14}\text{L}$ and 100 IP₃R receptors. The training data consists of simulations at IP₃ concentrations over $[0.4, 1]\mu\text{M}$ in intervals of $0.1\mu\text{M}$. Two subnet models are explored: a deep & wide subnet consisting of 8 layers of width 500 units, and a shallow & thin subnet consisting of a single layer of 25 units, both using ReLU activation functions and dropout. Three species are used in the effective probability distribution (4): Ca^{2+} , IP₃ and a latent species X . The reaction approximations used are those from enumerating the Lotka-Volterra system (Supplemental material): $P \rightarrow 2P$, $H \rightarrow \emptyset$, and $H + P \rightarrow 2H$, allowing each combination of $\{H, P\}$ from $\{\text{Ca}^{2+}, \text{IP}_3, X\}$.

To demonstrate how domain-specific knowledge improves generalization, a comparison *parameter-only model* is shown, equivalent to Figure 1 but missing the reaction approximations (Supplemental material). Both models are

trained using the Adam optimizer [20] with batch size 64 and learning rate 10^{-3} . The deep subnet is trained for 25 rounds with weight clipping beyond a cutoff magnitude of 5; the shallow subnet for 200 rounds and weight cutoff 1. Between the parameter-only and the *reaction model*, the latter generalizes better to IP_3 concentrations not observed during training. Further, the reaction model outperforms the comparison at keeping concentrations non-negative over the domain explored, although this is not explicitly enforced.

The generalization of the parameter-only model is better for the deep subnet than for the shallow subnet, partly because multiple layers of dropout improve generalization. However, the reaction model generalizes well even for the very low parameter shallow subnet. Figure 4(a) shows the integrated parameters at two slices of IP_3 using the Euler method. The reaction models learn the curves more exactly on both training and validation sets. This is quantified by a lower mean-squared error (MSE) shown in Figure 4(b).

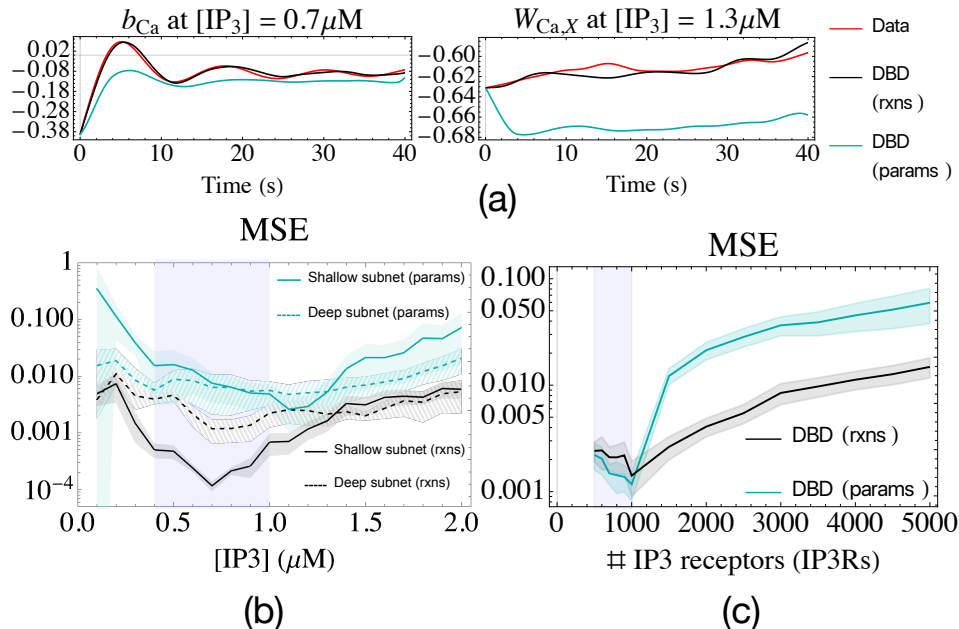


FIG. 4. (a) Parameters from the shallow subnet model from slices of Figure 3 at $[\text{IP}_3] = 0.7 \mu\text{M}$ and $[\text{IP}_3] = 1.3 \mu\text{M}$. The reaction model learns a more detailed model. (b) MSE for the learned parameters $\hat{\theta}$ in the models of Figure 3, with training data in blue. Models with reaction approximations decrease MSE by up to an order of magnitude. Shading shows 95% confidence intervals from 10 optimization trials. (c) MSE of a second model generalizing in IP_3 receptor number, with 95% confidence intervals from 40 trials, and training data in blue.

B. Encoding conservation

A second axis to generalize in is the number of IP_3Rs . The PCA model is now formulated for four species $\{\text{Ca}^{2+}, \text{IP}_3, \text{IP}_3\text{R}, X\}$ (the variance of IP_3R is set to a small constant 10^{-7} in the ML step). Since the receptor number is conserved in the simulations, the reaction approximations are extended with three of the form $A + \text{IP}_3\text{R} \rightarrow \text{IP}_3\text{R}$, where A is one of $\{\text{Ca}^{2+}, \text{IP}_3, X\}$. This explicitly conserves IP_3R in the input approximations.

Figure 4(c) shows the MSE over parameters for this model, trained on simulations at IP_3Rs over $[500, 1000]$ in intervals of 100. The reaction model outperforms the parameter-only model over the validation set covering 1000 to 5000 receptors. Training used the Adam optimizer for 25 rounds, with learning rate 10^{-3} and batch size 64. The subnet has 5 hidden layers of 150 units, ReLU activations, dropout rate 0.1, and weight cutoff 0.5.

IV. DISCUSSION

The power of DBDs is that knowledge of the domain can be explicitly built into the learning problem. This is possible due to the tight connection between reduced and fine scale models. Both are Markovian, depending only on the current point in parameter space. Moreover, because the reduced model is formulated by differential

equations (5), reaction network physics could be built in through candidate functions derived from the master equation. Additionally, conservation laws for IP₃R were included in the network inputs. These connections to the underlying physics differentiate DBDs from how neural networks are commonly used for time series regression, and other methods including hidden Markov models (HMMs) and recurrent neural networks (RNNs). A further desired property is that the learned covariance matrix $C(t)$ is positive semidefinite at all times. This is the case for the PCA model (7) due to the transformation (10), but not for a generic Gaussian distribution. Additionally, the means $\mu(t)$ should be non-negative to represent particle counts. This is not enforced explicitly, but is observed for the reaction models in Figure 3.

Other methods have been proposed that learn a neural network representing a differential equation directly from parameters without explicitly incorporating domain-specific physics [22, 28, 31]. A related method that uses candidates is SINDy [6], but its differential equations are linear and struggle with model reduction, where candidates do not include the true dynamics. Further, its candidates are arbitrary polynomial forms, and not necessarily connected to underlying physics. For graphical models, graph-constrained correlation dynamics (GCCD) [18] has used polynomial and exponential candidates non-linearly with neural networks. Parameterizations using basis functions from finite elements [13, 14] have also been used. In these cases, for graphical models other than PCA (7), the ML parameters can be estimated by the Boltzmann machine learning algorithm [1] or by expectation maximization [4].

One avenue for improvement is to include approximations for small networks rather than just individual reactions. DBDs may also be extendable to delay differential equations to improve regression performance. Alternatively, this may be implemented using tailored input reaction motifs. Further closure approximations beyond the Gaussian closure can also be included as candidates.

While the models considered have no spatial dependence, the approach is equally valid for spatial systems [12, 13]. A spatial model of IP₃-dependent calcium oscillations may include plasma membrane pumps and feedback on IP₃ production. One application of DBDs is to synaptic neuroscience, where simulations of signaling pathways [3] could be used to build models that are computationally efficient and generalize well to new stimulation patterns. Beyond reaction-diffusion systems, applications to other domains such as neural populations [26] may be possible.

ACKNOWLEDGMENTS

This work was supported by NIH R56-AG059602 (E.M., O.K.E., T.M.B., and T.J.S.), NIH P41-GM103712, NIH R01-MH115556 (O.K.E., T.M.B., and T.J.S.), Human Frontiers Science Program Grant No. HFSP-RGP0023/2018, the UC Irvine Donald Bren School of Information and Computer Sciences, NSF Grant No. PHY-1748958, NIH Grant No. R25GM067110, and the Gordon and Betty Moore Foundation Grant No. 2919.02 (E.M.).

-
- [1] David H. Ackley, Geoffrey E. Hinton, and Terrence J. Sejnowski. A learning algorithm for Boltzmann machines. *Cognitive Science*, 9(1):147–169, 1985.
 - [2] Nathan Baker, Frank Alexander, Timo Bremer, Aric Hagberg, Yannis Kevrekidis, Habib Najm, Manish Parashar, Abani Patra, James Sethian, Stefan Wild, Karen Willcox, and Steven Lee. Workshop report on basic research needs for scientific machine learning: Core technologies for artificial intelligence. Technical report, DOE Office of Science, 2 2019.
 - [3] Thomas M Bartol, Daniel X Keller, Justin P Kinney, Chandrajit L Bajaj, Kristen M Harris, Terrence J Sejnowski, and Mary B Kennedy. Computational reconstitution of spine calcium transients from individual proteins. *Frontiers in Synaptic Neuroscience*, 7:17, 2015.
 - [4] Christopher Bishop. *Pattern recognition and machine learning*. Springer, New York, 2006.
 - [5] Steve Branson, Grant Van Horn, Serge Belongie, and Pietro Perona. Bird species categorization using pose normalized deep convolutional nets. *arXiv:1406.2952*, 2014.
 - [6] Steven L. Brunton, Joshua L. Proctor, and J. Nathan Kutz. Discovering governing equations from data by sparse identification of nonlinear dynamical systems. *Proceedings of the National Academy of Sciences*, 113(15):3932–3937, 2016.
 - [7] Giuseppe Carleo and Matthias Troyer. Solving the quantum many-body problem with artificial neural networks. *Science*, 355(6325):602–606, 2017.
 - [8] Emmanuel de Bézenac, Arthur Pajot, and Patrick Gallinari. Deep learning for physical processes: incorporating prior scientific knowledge. *Journal of Statistical Mechanics: Theory and Experiment*, 2019(12):124009, dec 2019.
 - [9] G W De Young and J Keizer. A single-pool inositol 1,4,5-trisphosphate-receptor-based model for agonist-stimulated oscillations in Ca²⁺ concentration. *Proc Natl Acad Sci U S A*, 89(20):9895–9899, Oct 1992.
 - [10] Dennis Decoste and Bernhard Schölkopf. Training invariant support vector machines. *Mach. Learn.*, 46(1–3):161–190, March 2002.
 - [11] Oliver Ernst, Tom Bartol, Terrence Sejnowski, and Eric Mjolsness. Code for: Physics-based machine learning for modeling IP₃ induced calcium oscillations. 10.5281/zenodo.4839127, May 2021.

- [12] Oliver K. Ernst, Tom Bartol, Terrence Sejnowski, and Eric Mjolsness. Learning dynamic Boltzmann distributions as reduced models of spatial chemical kinetics. *The Journal of Chemical Physics*, 149(3):034107, 2018.
- [13] Oliver K. Ernst, Thomas M. Bartol, Terrence J. Sejnowski, and Eric Mjolsness. Learning moment closure in reaction-diffusion systems with spatial dynamic boltzmann distributions. *Phys. Rev. E*, 99:063315, Jun 2019.
- [14] Oliver K. Ernst, Tom Bartol, Terrence Sejnowski, and Eric Mjolsness. Deep learning moment closure approximations using dynamic boltzmann distributions. *arXiv:1905.12122*, 2019.
- [15] Daniel T. Gillespie. Exact stochastic simulation of coupled chemical reactions. *The Journal of Physical Chemistry*, 81(25):2340–2361, 1977.
- [16] Taira Giordani, Alessia Suprano, Emanuele Polino, Francesca Acanfora, Luca Innocenti, Alessandro Ferraro, Mauro Paternostro, Nicolò Spagnolo, and Fabio Sciarrino. Machine learning-based classification of vector vortex beams. *Phys. Rev. Lett.*, 124:160401, Apr 2020.
- [17] Raban Iten, Tony Metger, Henrik Wilming, Lídia del Rio, and Renato Renner. Discovering physical concepts with neural networks. *Phys. Rev. Lett.*, 124:010508, Jan 2020.
- [18] Todd Johnson, Tom Bartol, Terrence Sejnowski, and Eric Mjolsness. Model reduction for stochastic CaMKII reaction kinetics in synapses by graph-constrained correlation dynamics. *Physical Biology*, 12(4):045005–045005, 07 2015.
- [19] Rex A Kerr, T M Bartol, Boris Kaminsky, Markus Dittrich, Jen-Chien Jack Chang, Scott B Baden, Terrence Sejnowski, and J R Stiles. Fast Monte Carlo simulation methods for biological reaction-diffusion systems in solution and on surfaces. *SIAM Journal on Scientific Computing : a publication of the Society for Industrial and Applied Mathematics*, 30(6):3126–3126, 10 2008.
- [20] Diederik P Kingma and Jimmy Ba. Adam: A method for stochastic optimization. *arXiv:1412.6980*, 2014.
- [21] S. C. Leemann, S. Liu, A. Hexemer, M. A. Marcus, C. N. Melton, H. Nishimura, and C. Sun. Demonstration of machine learning-based model-independent stabilization of source properties in synchrotron light sources. *Phys. Rev. Lett.*, 123:194801, Nov 2019.
- [22] Zichao Long, Yiping Lu, Xianzhong Ma, and Bin Dong. PDE-net: Learning PDEs from data. In Jennifer Dy and Andreas Krause, editors, *Proceedings of the 35th International Conference on Machine Learning*, volume 80 of *Proceedings of Machine Learning Research*, pages 3208–3216. PMLR, 10–15 Jul 2018.
- [23] Easwar Magesan, Jay M. Gambetta, A. D. Córcoles, and Jerry M. Chow. Machine learning for discriminating quantum measurement trajectories and improving readout. *Phys. Rev. Lett.*, 114:200501, May 2015.
- [24] Daniel C. Mattis and M. Lawrence Glasser. The uses of quantum field theory in diffusion-limited reactions. *Rev. Mod. Phys.*, 70:979–1001, Jul 1998.
- [25] Eric Mjolsness and Dennis DeCoste. Machine learning for science: State of the art and future prospects. *Science*, 293(5537):2051–2055, 2001.
- [26] Toru Ohira and Jack D. Cowan. *Stochastic Neurodynamics and the System Size Expansion*, pages 290–294. Springer US, Boston, MA, 1997.
- [27] Evan Racah, Christopher Beckham, Tegan Maharaj, Samira Ebrahimi Kahou, Prabhat, and Christopher Pal. Extreme weather: A large-scale climate dataset for semi-supervised detection, localization, and understanding of extreme weather events. In *Proceedings of the 31st International Conference on Neural Information Processing Systems, NIPS’17*, pages 3405–3416, Red Hook, NY, USA, 2017. Curran Associates Inc.
- [28] Maziar Raissi, Paris Perdikaris, and George Em Karniadakis. Multistep neural networks for data-driven discovery of nonlinear dynamical systems. *arXiv:1801.01236*, 2018.
- [29] Matthias Rupp, Alexandre Tkatchenko, Klaus-Robert Müller, and O. Anatole von Lilienfeld. Fast and accurate modeling of molecular atomization energies with machine learning. *Phys. Rev. Lett.*, 108:058301, Jan 2012.
- [30] Andrew W Senior, Richard Evans, John Jumper, James Kirkpatrick, Laurent Sifre, Tim Green, Chongli Qin, Augustin Židek, Alexander W R Nelson, Alex Bridgland, Hugo Penedones, Stig Petersen, Karen Simonyan, Steve Crossan, Pushmeet Kohli, David T Jones, David Silver, Koray Kavukcuoglu, and Demis Hassabis. Improved protein structure prediction using potentials from deep learning. *Nature*, 577(7792):706–710, 2020.
- [31] Thomas N Thiem, Mahdi Kooshkbaghi, Tom Bertalan, Carlo R Laing, and Ioannis G Kevrekidis. Emergent spaces for coupled oscillators. *Frontiers in computational neuroscience*, 14:36–36, 05 2020.
- [32] V. Voorluijs, S. Ponce Dawson, Y. De Decker, and G. Dupont. Deterministic limit of intracellular calcium spikes. *Phys. Rev. Lett.*, 122:088101, Feb 2019.
- [33] D. Xiao, L. Marin, and Rick Chartrand. Numerical differentiation of noisy, nonsmooth data. *ISRN Applied Mathematics*, 2011:164564, 2011.

Appendix A: Code

All code is available as part of this supplemental material as well as online [11]. This includes codes for the stochastic simulations, learning problems, and notebooks to reproduce figures. See the “Readme” files included with the code for directions.

Appendix B: IP₃ dependent calcium oscillations

1. Stochastic models

Figure 2 of the main text shows a schematic of the model of IP₃ dependent calcium oscillations in non-excitable cells. Clusters of IP₃ receptors (IP₃Rs) in the membrane of the endoplasmic reticulum are activated by cytosolic calcium and IP₃, allowing transport through the channel into the cytoplasm. The channel model for a single IP₃ receptor subunit is shown in Figure 5. While the receptor is known to be composed of four subunits, the peak conductance is observed when only three are open. Hence, the original model of De Young and Keizer [9] considers only three subunits. The reactions in the receptor subunit are:



where the open state is S_{110} . Table I gives the parameter values used for stochastic simulations, which are the same values used in the original De Young and Keizer [9] model. The molecular-based reaction rates are obtained from the concentration-based rates as:

$$\begin{aligned}
 \alpha_i &= \frac{a_i}{c_A \times V_{\text{Cyt}}}, \\
 \beta_i &= b_i,
 \end{aligned} \tag{B2}$$

as derived in Section B 3, where c_A is Avogadro's constant and V_{Cyt} is the volume of the cytoplasm.

Transport through the channel is given by the reactions:



as also derived in Section B 3 from the differential equation model by De Young and Keizer [9].

The recovery of calcium from the cytoplasm is attributed to ATP-driven pumps such as SERCA pumps. In this model, since the density of these pumps is as high as $1000/\mu\text{m}^2$ [3] and the ER is a highly folded structure with a large surface area, this process is not modeled using stochastic particle-based methods, but rather by differential equations:

$$\begin{aligned}
 \frac{d[\text{Ca}_{\text{Cyt}}]}{dt} &= J_1 - J_2, \\
 J_1 &= c_1 v_2 (c_1^{-1} [\text{Ca}_{\text{ER}}] - [\text{Ca}_{\text{Cyt}}]), \\
 J_2 &= \frac{v_3 [\text{Ca}_{\text{Cyt}}]^2}{[\text{Ca}_{\text{Cyt}}]^2 + k_3^2},
 \end{aligned} \tag{B4}$$

where J_1 is a leak current, and J_2 is the ATP-driven recovery of calcium back to the ER. See also Section B 3.

Examples of the stochastic simulations are shown in Figure 6. The initial number of Ca^{2+} and IP₃ are sampled from the Gaussian distributions:

$$\begin{aligned}
 [\text{Ca}_{\text{Cyt}}]_0 &= \mathcal{N}(\mu_0([\text{Ca}_{\text{Cyt}}]), \sigma_0^2([\text{Ca}_{\text{Cyt}}])), \\
 [\text{IP}_3]_0 &= \mathcal{N}(\mu_0([\text{IP}_3]), \sigma_0^2([\text{IP}_3])),
 \end{aligned} \tag{B5}$$

where the parameter values are given in Table I.

After sampling the initial counts, an initial simulation is used to initialize the states of the IP₃ receptors. Let the numbers of particles corresponding to the concentrations (B5) be $n_{\text{Ca}_{\text{Cyt}},0}$ and $n_{\text{IP}_3,0}$, from which the number of calcium particles in the ER $n_{\text{Ca}_{\text{ER}},0}$ can be calculated using c_0, c_1 . The IP₃R are initialized to the specified and fixed number $n_{\text{IP}_3\text{R}}$ of receptors, all in state S_{000} , and all other receptor states S_{ijk} with population zero. The initial simulation is

run with only the IP₃R state reaction system (B1), and where the number of Ca_{Cyt}, IP₃, Ca_{ER} is conserved, i.e. fixed to their initial values. The duration of the initial simulation is 10 s. From this, the initial states of the receptors are taken for the main simulation as the average state values over the last 4 s of the initial simulation.

The main simulations are run from $t = 0$ to $t = T_{\max}$, with the count of each species written out at intervals $\Delta t^{(\text{write})}$. The currents from the differential equations (B4) are updated at short time intervals $\Delta t^{(\text{diff. eq.})}$, with all parameters as given in Table I.

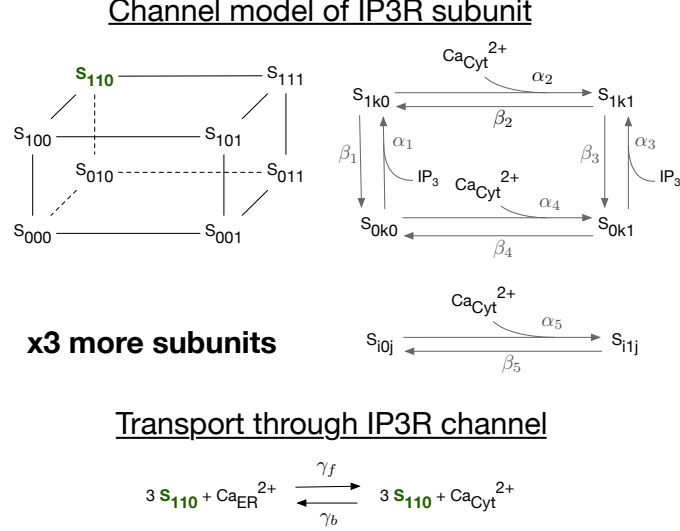


FIG. 5. Channel models for the IP₃R and transport through the channel, which is open when one calcium ion and one IP₃ are bound. A further calcium binding inhibits the channel. Peak conductance is observed when three subunits are open; a fourth that is physically observed is not modelled. The open state is S₁₁₀, indicated in green.

2. Range of oscillations

Figure 5 shows the original bifurcation diagram by De Young and Keizer [9], and the range of oscillations in the stochastic model under consideration. The stochastic curves should not be interpreted as a bifurcation diagram. Rather, at each concentration of IP₃:

- At each timepoint, average over stochastic simulations to obtain the mean $\mu(t)$ and standard deviation $\sigma(t)$.
- Calculate the upper and lower curves over time $c_{\pm}(t) = \mu(t) \pm \sigma(t)$.
- Take the min. and max.:

$$\begin{aligned} c_{-, \min} &= \min_t(c_-(t)), \\ c_{+, \max} &= \max_t(c_+(t)), \end{aligned} \tag{B6}$$

over the last 40s of each of the 100s simulations.

The resulting $c_{-, \min}, c_{+, \max}$ are plotted in Figure 5 to indicate the range of oscillations. Error bars indicate 95% confidence levels.

3. Derivation of reaction model from differential equations

The original differential equations in De Young and Keizer [9] are:

$$\frac{d[\text{Ca}_{\text{Cyt}}^{2+}]_{\text{Cyt}}}{dt} = J_1 - J_2 + J_3, \tag{B7}$$

TABLE I. Parameter values used for stochastic simulations.

Parameter	Value	Description
c_0	$2 \mu\text{M}$	Total [Ca] in terms of cytosolic volume
c_1	0.185	Ratio ER volume to cytosol volume
v_1	6 s^{-1}	Max Ca channel flux
v_2	0.11 s^{-1}	Ca leak flux constant
v_3	$0.9 (\mu\text{M} \times \text{s})^{-1}$	Max Ca uptake
k_3	$0.1 \mu\text{M}$	Activation constant for ATP-Ca pump
a_1	$400 (\mu\text{M} \times \text{s})^{-1}$	IP ₃ R reaction rate
a_2	$0.2 (\mu\text{M} \times \text{s})^{-1}$	IP ₃ R reaction rate
a_3	$400 (\mu\text{M} \times \text{s})^{-1}$	IP ₃ R reaction rate
a_4	$0.2 (\mu\text{M} \times \text{s})^{-1}$	IP ₃ R reaction rate
a_5	$20 (\mu\text{M} \times \text{s})^{-1}$	IP ₃ R reaction rate
d_1	$0.13 \mu\text{M}$	IP ₃ R reaction rate
d_2	$1.049 \mu\text{M}$	IP ₃ R reaction rate
d_3	$943.4 \times 10^{-3} \mu\text{M}$	IP ₃ R reaction rate
d_4	$144.5 \times 10^{-3} \mu\text{M}$	IP ₃ R reaction rate
d_5	$82.34 \times 10^{-3} \mu\text{M}$	IP ₃ R reaction rate
$\mu_0([\text{Ca}_{\text{Cyt}}])$	$0.25 \mu\text{M}$	Initial mean Ca concentration
$\mu_0([\text{IP}_3])$	Varying	Initial mean IP ₃ concentration
$\sigma_0([\text{Ca}_{\text{Cyt}}])$	$10^{-3} \mu\text{M}$	Initial standard deviation of Ca concentration
$\sigma_0([\text{IP}_3])$	$10^{-3} \mu\text{M}$	Initial standard deviation of IP ₃ concentration
V_{Cyt}	10^{-12} or 10^{-14} L	Cytoplasm volume
$\Delta t^{(\text{write})}$	0.1 s	Writing interval
$\Delta t^{(\text{diff. eq.})}$	0.001 s	Integration step length for currents
T_{max}	50 s	Maximum simulation time

where

$$\begin{aligned}
J_1 &= c_1 v_2 (c_1^{-1} [\text{Ca}_{\text{ER}}^{2+}]_{\text{Cyt}} - [\text{Ca}_{\text{Cyt}}^{2+}]_{\text{Cyt}}), \\
J_2 &= \frac{v_3 [\text{Ca}_{\text{Cyt}}^{2+}]_{\text{Cyt}}^2}{[\text{Ca}_{\text{Cyt}}^{2+}]_{\text{Cyt}}^2 + k_3^2}, \\
J_3 &= c_1 v_1 x_{110}^3 (c_1^{-1} [\text{Ca}_{\text{ER}}^{2+}]_{\text{Cyt}} - [\text{Ca}_{\text{Cyt}}^{2+}]_{\text{Cyt}}),
\end{aligned} \tag{B8}$$

where x_{110} is the fraction of subunits in the open state S_{110} , and c_1, v_1, v_2, v_3, k_3 are constants given in Table I. The current J_1 is a leak current, J_2 is the flux out of cytoplasm due to an ATP-dependent Ca^{2+} pump, e.g. a SERCA pump, and J_3 is the transport of Ca^{2+} into cytoplasm through the open IP₃R. The notation $[X_{\text{ER}}]_{\text{Cyt}}$ is used to denote the number of particles of species X located in the ER, divided by the volume of Cyt to obtain a concentration (as opposed to the volume of the ER). This conversion is used to simplify the calculations by having to keep track of only a single volume.

The currents J_1, J_2 are kept as differential equations, while the transport J_3 is converted to an equivalent reaction system. For this transformation, *concentration-based* reaction rates must be transformed into *molecular-based* reaction rates.

Consider a general reaction of the form:



Associated with this reaction is the stoichiometry vector ν of length R , whose components ν_i describe the change in the number of particles of X_i . Here, γ will be referred to as the molecular-based reaction rate. The goal is to relate γ

to the concentration-based reaction rate k appearing in mass action kinetics:

$$\frac{d[X_j]}{dt} = -\nu_j k \prod_{i=1}^R ([X_i])^{m_i} + \dots, \quad (\text{B10})$$

where the \dots denote other possible reactions.

The propensity term for the reaction (B9) in units of molecules per time is:

$$\rho = \gamma \prod_{i=1}^R \binom{n_{X_i}}{m_i}. \quad (\text{B11})$$

where n_{X_i} is the number of particles of species X_i . At large particle numbers, this is commonly approximated by

$$\rho \approx \gamma \prod_{i=1}^R \frac{n_{X_i}^{m_i}}{m_i!}. \quad (\text{B12})$$

In the mass action equation (B10), the reaction-based rate of change in units of concentration per time is (without the stoichiometry vector):

$$k \prod_{i=1}^R ([X_i])^{m_i}. \quad (\text{B13})$$

Substitute the definition of the concentration $[X_i] = n_{X_i}/(c_A \times V)$ for n_{X_i} particles in volume V where c_A is Avogadro's constant, and convert to units of molecules per time by multiplying by $c_A \times V$:

$$k c_A V \prod_{i=1}^R \left(\frac{n_{X_i}}{c_A V} \right)^{m_i}. \quad (\text{B14})$$

Equating this with the approximation for the propensity (B12) gives the relation:

$$\gamma = k c_A V \prod_{i=1}^R \frac{m_i!}{(c_A V)^{m_i}}. \quad (\text{B15})$$

Using this relation, the transport current J_3 can be transformed by writing it in the equivalent form:

$$\begin{aligned} J_3 &= k_{1f} [S_{110}]_{\text{Cyt}}^3 [\text{Ca}_{\text{ER}}^{2+}]_{\text{Cyt}} - k_{1b} [S_{110}]_{\text{Cyt}}^3 [\text{Ca}_{\text{Cyt}}^{2+}]_{\text{Cyt}}, \\ k_{1f} &= v_1 [\text{IP}_3\text{R}]_{\text{Cyt}}^{-3}, \\ k_{1b} &= c_1 v_1 [\text{IP}_3\text{R}]_{\text{Cyt}}^{-3}. \end{aligned} \quad (\text{B16})$$

where S_{110} is the open state of the IP_3R in Figure 5. From this the equivalent reaction can be identified:



where the molecular-based rates are given by (B15):

$$\begin{aligned} \gamma_{1f} &= 6v_1 n_{\text{IP}_3\text{R}}^{-3}, \\ \gamma_{1b} &= 6c_1 v_1 n_{\text{IP}_3\text{R}}^{-3}, \end{aligned} \quad (\text{B18})$$

where $n_{\text{IP}_3\text{R}}$ is the number of IP_3R .

4. Number of IP_3 receptor subunits

The number of IP_3 receptors (IP_3R) depends on the density of channels and the surface area of the ER. The ER is a highly folded structure, and as such its surface area can vary significantly. In the text a large spread in the number of channels is explored. Here, an order of magnitude estimation is provided to justify their scale.

Starting with the volume of the cytoplasm V_{cyt} , the volume of the ER is $V_{\text{ER}} = c_1 \times V_{\text{cyt}}$ where $c_1 = 0.185$ is the ratio estimated in De Young and Keizer [9]. The ER has the smallest surface area if it is a sphere:

$$\text{SA}_{\text{ER}}^{\text{min}} = 4\pi \left(\frac{3}{4\pi} V_{\text{ER}} \right)^{2/3}. \quad (\text{B19})$$

Let the actual surface area be some factor λ larger than the minimum:

$$\text{SA}_{\text{ER}} = \lambda \times \text{SA}_{\text{ER}}^{\text{min}}. \quad (\text{B20})$$

IP₃R clusters are spread out over the ER with spacing $1 - 7\mu\text{m}$ [32]. Assuming the IP₃R clusters were located in a grid with spacing $\Delta x_{\text{IP3R clusters}}$ gives:

$$n_{\text{IP3R clusters}} = \frac{\text{SA}_{\text{ER}}}{\Delta x_{\text{IP3R clusters}}^2}. \quad (\text{B21})$$

Each cluster contains up to 15 channels [32]. Assuming 10 channels per cluster and with 4 subunits per channel gives:

$$n_{\text{IP3R subunits}} = 10 \times 4 \times n_{\text{IP3R clusters}} = \frac{160\pi\lambda}{\Delta x_{\text{IP3R clusters}}^2} \left(\frac{3}{4\pi} c_1 V_{\text{cyt}} \right)^{2/3}. \quad (\text{B22})$$

Figure 7 shows the number of IP₃R subunits for a range of spacings and surface area factors. For a highly folded ER with large λ and average cluster spacing $\Delta x_{\text{IP3R clusters}} \sim 3\mu\text{m}$, the estimates of $\mathcal{O}(100)$ subunits for $\text{Vol}_{\text{cyt}} = 10^{-14}L$ and $\mathcal{O}(1000)$ subunits for $\text{Vol}_{\text{cyt}} = 10^{-12}L$ are reasonable, which are the approximate magnitudes explored in the text.

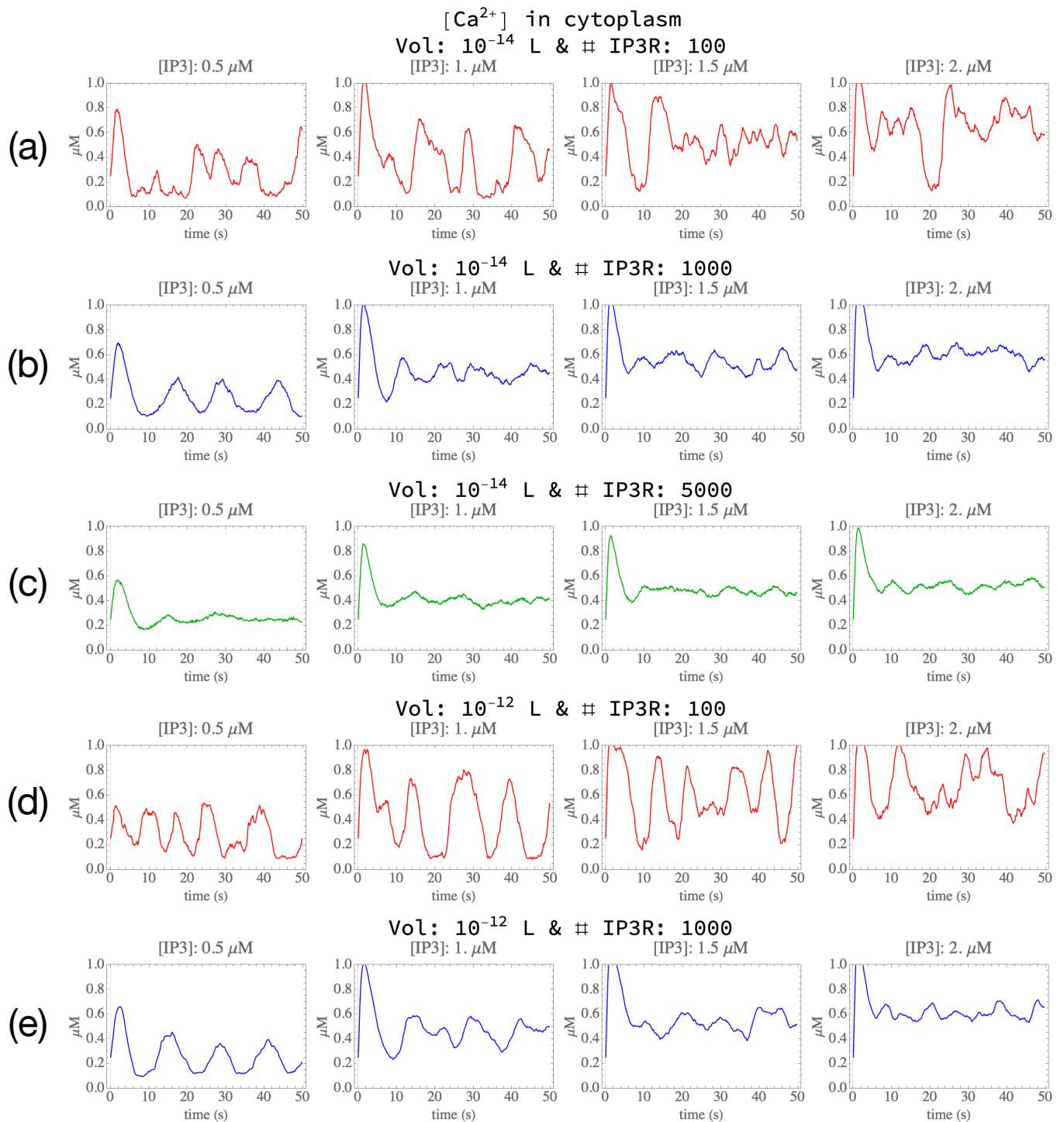


FIG. 6. Stochastic simulations of cytosolic calcium oscillations for (a) 100 IP₃R and (b) 1000 IP₃R at various IP₃ concentrations and cytoplasm volume of 10⁻¹⁴L. Calcium spikes are observed at all concentrations, and are more pronounced at lower receptor number.

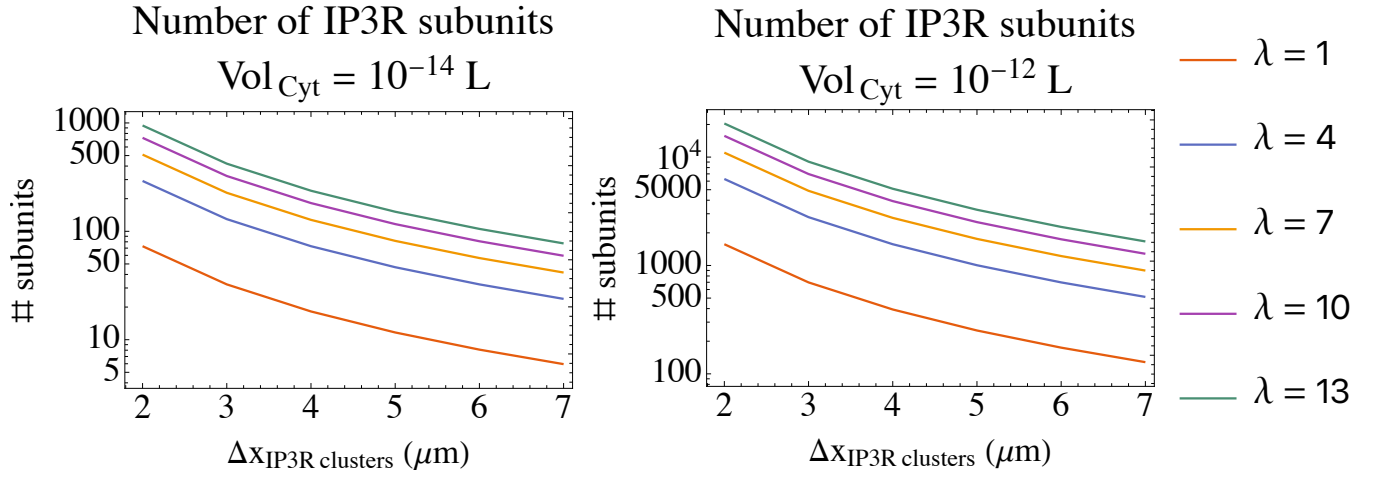


FIG. 7. Number of IP3R subunits given by (B22) as a function of the cluster spacing $\Delta x_{\text{IP3R clusters}}$ in μm , and the dimensionless surface area factor λ , where $\lambda = 1$ corresponds to a sphere.

Appendix C: Training ML models

1. Data transformation

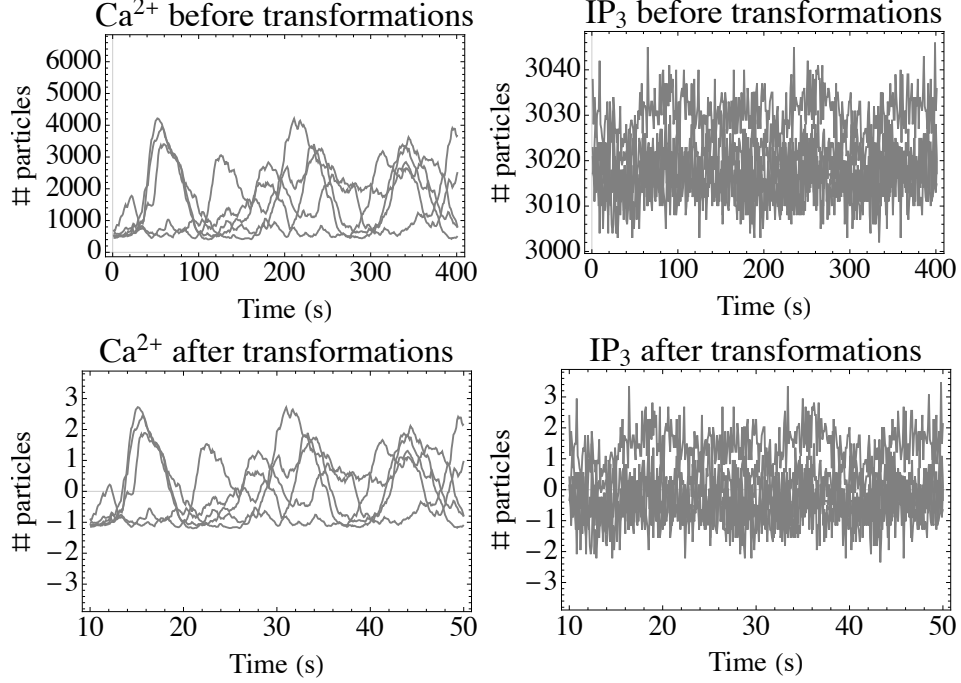


FIG. 8. Example standardizing transformation for the system studied in Figure 3 of the main text at $[\text{IP}_3] = 0.5\mu\text{M}$. Five stochastic simulation trajectories are shown in gray. *Top row*: Number of particles of calcium and IP_3 before transformation. *Bottom row*: After transformation, oscillations occur around zero.

Let the stochastic simulation data be represented by the matrix $X(t)$ of size $M \times N_v$ where N_v is the dimension of the visible variables and M is the number of samples:

$$X(t) = \begin{pmatrix} \mathbf{x}_1^\top(t) \\ \mathbf{x}_2^\top(t) \\ \dots \\ \mathbf{x}_M^\top(t) \end{pmatrix}. \quad (\text{C1})$$

PCA applied to $X(t)$ leads to the parameters:

$$\hat{\boldsymbol{\theta}}_X(t) = \{\hat{\mathbf{b}}_X, \hat{W}_X, \sigma_X^2\}(t). \quad (\text{C2})$$

From these parameters, approximations $\hat{\mathbf{F}}_{\text{rxn.}}^{(\text{approx.})}$ to $\hat{\mathbf{F}}$ under different reaction processes can be calculated.

When using the model to integrate the parameters $\hat{\boldsymbol{\theta}}_X(t)$, it traces out a trajectory in $\hat{D} = N_v + N_v \times N_h + 1$ dimensional space. In order for this integration to be stable, the inputs to the neural network $\hat{\mathbf{F}}_{\text{rxn.}}^{(\text{approx.})}$ must not be sensitive to small perturbations in $\hat{\boldsymbol{\theta}}_X(t)$. Note that the error in $\hat{\boldsymbol{\theta}}_X(t)$ is set by the error in the output of the neural network, and the integration drift that arises from integrating a noisy signal.

To ensure that the Jacobian $\partial \hat{\mathbf{F}}_{\text{rxn.}}^{(\text{approx.})} / \partial \hat{\boldsymbol{\theta}}_X(t)$ is small, introduce the following transformation. For a given trajectory $\mathbf{x}_i(t), i = 1, \dots, M$, compute the mean and variance over time and samples:

$$\begin{aligned} \mathbf{m} &= \frac{1}{T} \sum_{t=1}^T \frac{1}{M} \sum_{i=1}^M \mathbf{x}_i(t), \\ \mathbf{v} &= \frac{1}{T} \sum_{t=1}^T \frac{1}{M} \sum_{i=1}^M [\mathbf{x}_i(t) - \mathbf{m}]^2, \end{aligned} \quad (\text{C3})$$

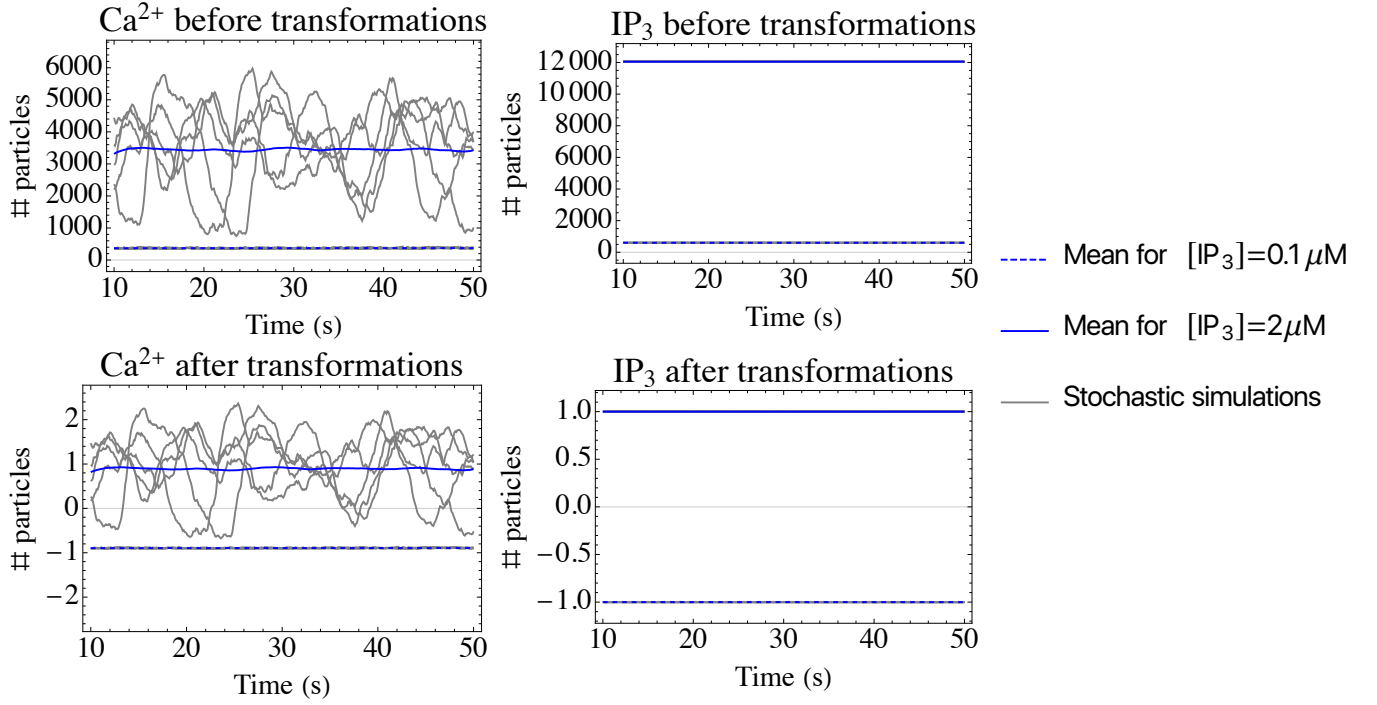


FIG. 9. Transformations for the IP_3 system studied in Figure 3 of the main text. The transformation is calculated for stochastic simulations at the upper and lower range of oscillations considered, i.e. $[\text{IP}_3] = 0.1 \mu\text{M}$ and $[\text{IP}_3] = 2 \mu\text{M}$.

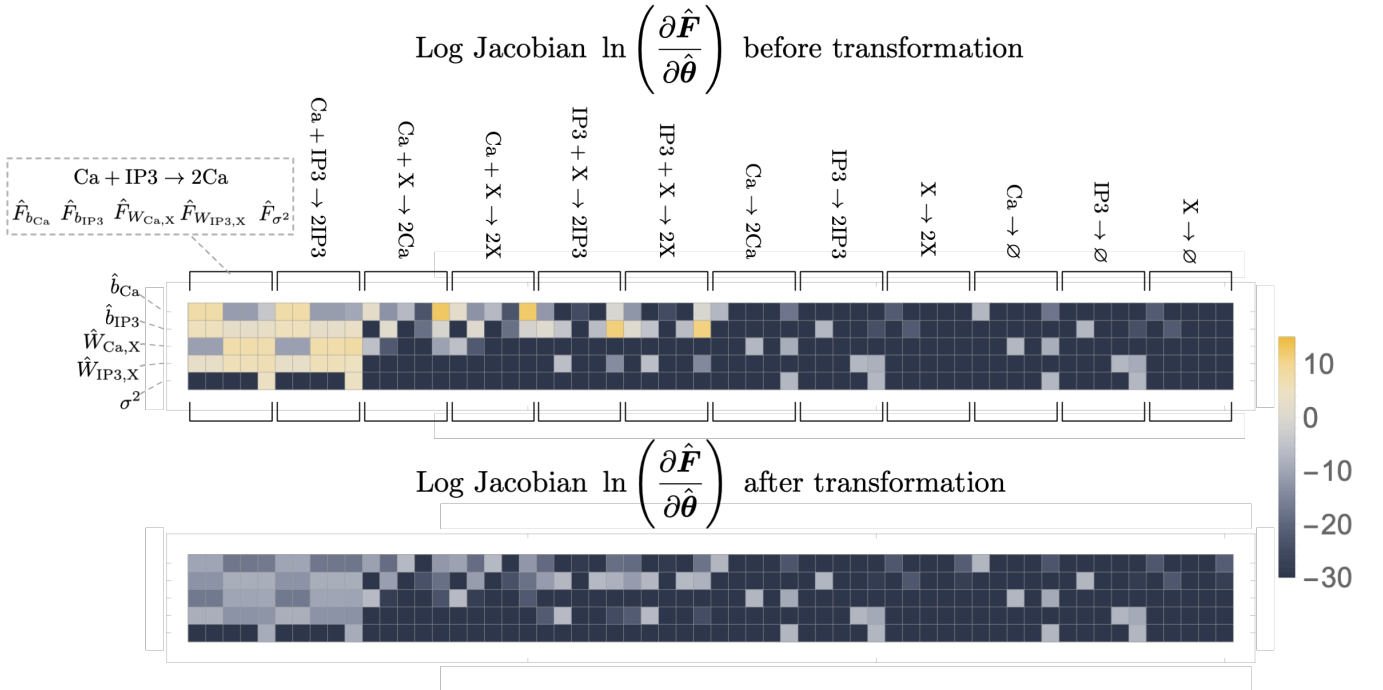


FIG. 10. Jacobian of reaction candidates with respect to standard parameters, plotted on a log scale. The reactions are those of the model studied in Figure 3 of the main text, and parameters $\hat{\theta}$ are those at a single point in time $t = 50$ and $[\text{IP}_3] = 0.7 \mu\text{M}$, with $\mu_h = 0$ and $\Sigma_h = I$. *Top*: Jacobian before the transformation (C4). *Bottom*: Jacobian after the transformation. The transformation reduces the Jacobian, increasing the stability of the integration because small perturbations do not significantly alter the inputs to the neural network.

and use these parameters to define a transformation:

$$\mathbf{y}_i(t) = \frac{\mathbf{x}_i(t) - \mathbf{m}}{\sqrt{\mathbf{v}}}. \quad (\text{C4})$$

This leads to a new matrix $Y(t)$ of equal size $M \times N_v$. PCA applied to $Y(t)$ leads to a different set of parameters:

$$\hat{\boldsymbol{\theta}}_Y(t) = \{\hat{\mathbf{b}}_Y, \hat{W}_Y, \sigma_Y^2\}(t). \quad (\text{C5})$$

Figure 8 shows how such a transformation standardizes oscillations. Figure 9 shows the transformation for the system studied in Figure 3 of the main text. Here the averages in (C3) are taken over IP_3 concentrations at the boundaries of the bifurcation diagram studied, i.e. at $[\text{IP}_3] = 0.1\mu\text{M}$ and $[\text{IP}_3] = 2\mu\text{M}$.

It is difficult to relate $\boldsymbol{\theta}_Y(t)$ to $\boldsymbol{\theta}_X(t)$ since it relates the eigendecomposition of a matrix product. Importantly, however, Figure 10 shows that the Jacobian $\partial \hat{\mathbf{F}}_{\text{rxn.}}^{\text{(approx.)}} / \partial \hat{\boldsymbol{\theta}}(t)$ has decreased for the example problem studied in Figure 3 of the main text.

2. Training inputs and targets

After transforming the data $X \rightarrow Y$, the ML parameters are identified from $Y(t)$ for $t = 1, \dots, T$ using Equation (9) of the main text. For the models considered in this work in Figure 3 of the main text and Figure 4 of the main text, the data used are in the range 10s to 50s of the stochastic simulations, which are of length 50s. The first 10s are discarded to lessen the dependence of the oscillations on the chosen initial condition in Table I. The parameters obtained are the standard parameters $\hat{\boldsymbol{\theta}}(t)$. Note that the sign of the eigenvectors is adjusted to be consistent by ensuring that for any eigenvector \mathbf{u} we have $|\cos^{-1}(\mathbf{u}^\top \mathbf{1})| \leq \pi/2$.

The targets derivatives are calculated from $\hat{\boldsymbol{\theta}}(t)$ using total variation regularization (TVR) [33]. For a time series \mathbf{z} with elements z_1, z_2, \dots, z_T , the time derivative $\dot{\mathbf{z}}$ is obtained by solving the optimization problem:

$$\dot{\mathbf{z}} = \min_{\mathbf{u}} \left(\alpha \|\dot{\mathbf{u}}\|_1 + \frac{1}{2} \|A\mathbf{u} - \mathbf{z}\|_2 \right), \quad (\text{C6})$$

where A is the anti-differentiation matrix, and α is a regularization parameter. In this case, the A matrix is that of the Euler method. The optimization problem is solved using the lagged diffusivity method [33] for 10 optimization steps for every parameter \mathbf{z} in $\hat{\boldsymbol{\theta}}$ with regularization parameter $\alpha = 100$. Additionally, after calculating the derivatives $d\hat{\boldsymbol{\theta}}/dt$, small derivative values with an absolute value below 10^{-5} are set to zero. The target outputs $d\hat{\boldsymbol{\theta}}/dt$ are therefore obtained:

$$\text{Target}(t) = \frac{d\hat{\boldsymbol{\theta}}(t)}{dt} = \begin{pmatrix} d\hat{\mathbf{b}}/dt \\ d\hat{W}/dt \\ d\sigma^2/dt \end{pmatrix}. \quad (\text{C7})$$

The inputs are obtained by integrating $d\hat{\boldsymbol{\theta}}/dt$ with the anti-differentiation matrix A to obtain smoothed inputs $\hat{\boldsymbol{\theta}}^{(\text{integrated})}$:

$$\text{Input}(t) = \hat{\boldsymbol{\theta}}^{(\text{integrated})}(t) = \begin{pmatrix} \hat{\mathbf{b}}(t) \\ \hat{W}(t) \\ \sigma^2(t) \end{pmatrix}. \quad (\text{C8})$$

3. Reaction approximations

The physics of the system is described by the chemical master equation (CME). The CME can be incorporated into the inference problem by using it to derive an approximation to the time evolution of parameters. Figure 11 shows a schematic of how this derivation as follows.

For the distribution defined by the current parameters $\boldsymbol{\theta}(t) = \{\mathbf{b}, W, \sigma^2, \boldsymbol{\mu}_h, \Sigma_h\}(t)$ at an instant in time, Equation (7) of the main text gives the observables $\boldsymbol{\phi}(t) = \{\boldsymbol{\mu}, C\}(t)$. Next, consider for example the predator-prey reaction

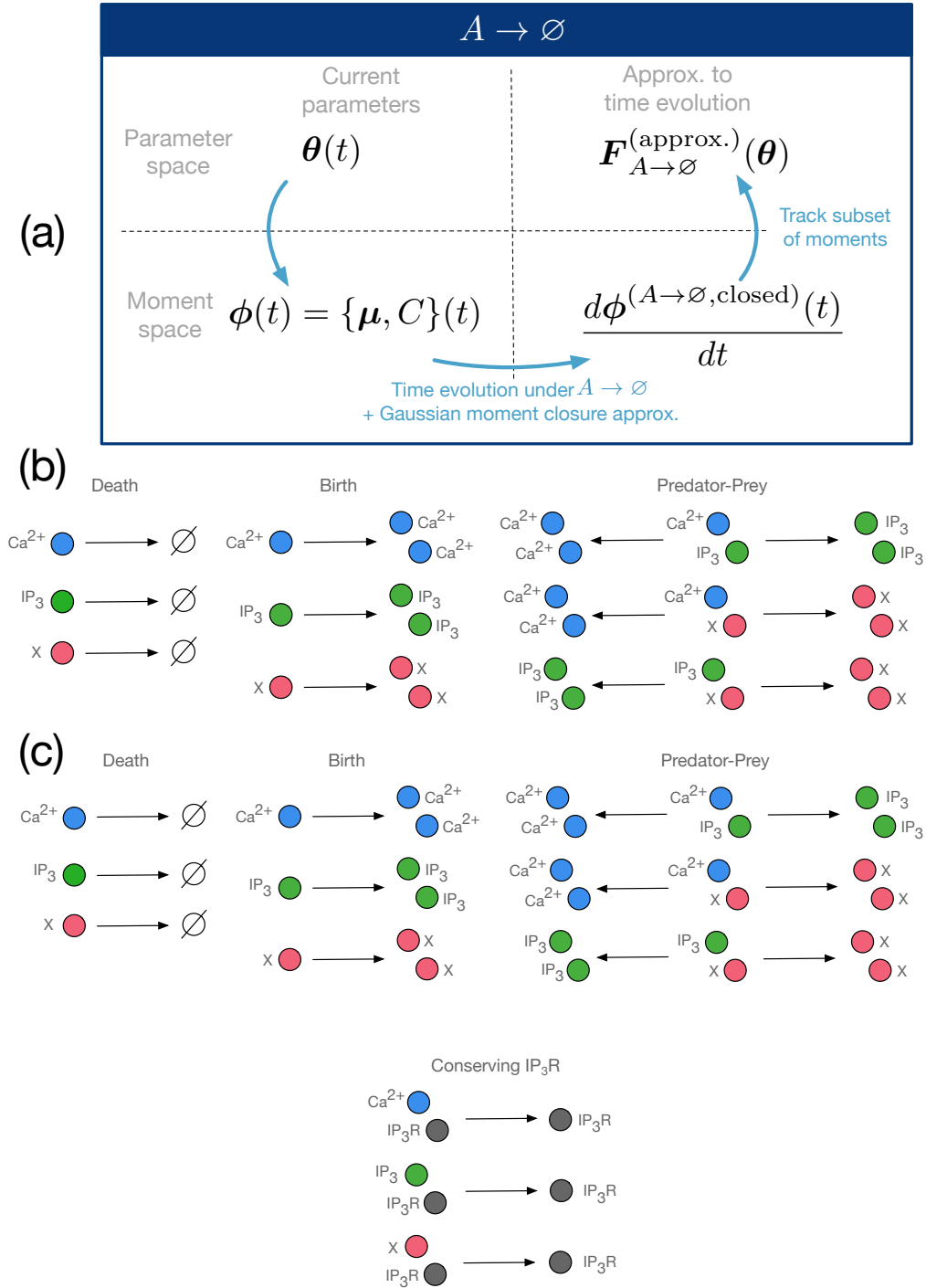


FIG. 11. (a) Schematic of how an approximation to the time evolution of parameters is derived for a single reaction pathway. The observables $\phi(t)$ corresponding to the distribution defined by the current parameters $\theta(t)$ at an instant in time are obtained from Equation (7) of the main text. The time evolution of each observable is calculated from the master equation, and closed using a Gaussian moment closure approximation (Equation (3) of the main text). By tracking exactly only a subset of moments $d\{\mu_v, \Sigma_{vh}, \text{Tr}(\Sigma_v), \mu_h, \Sigma_h\}/dt$ matching the dimensions of $\theta(t) = \{\mathbf{b}, W, \sigma^2, \mu_h, \Sigma_h\}(t)$, an approximation to the time evolution of the parameters is obtained. (b) The reactions used to construct the inputs to the sub-network models in Figure 3 of the main text generalizing in IP_3 : death e.g. $H \rightarrow \emptyset$, birth e.g. $P \rightarrow 2P$, and a predator-prey interaction, e.g. $H + P \rightarrow 2H$. These reactions mimic the reaction scheme of Lotka-Volterra system. Each combination of $\{H, P\}$ from $\{\text{Ca}^{2+}, \text{IP}_3, X\}$ is included. (c) The reactions used in the models including IP_3R . The reactions are those of (b), including three extra reactions for IP_3R that explicitly conserve IP_3R .

$H + P \rightarrow 2H$ with rate k for predators H and prey P . Under this reaction, the observables evolve in time according to:

$$\begin{aligned}\frac{d\langle n_P \rangle}{dt} &= -k\langle n_H n_P \rangle, \\ \frac{d\langle n_H \rangle}{dt} &= k\langle n_H n_P \rangle,\end{aligned}\tag{C9}$$

and

$$\begin{aligned}\frac{d\langle n_P^2 \rangle}{dt} &= -2k\langle n_H n_P^2 \rangle + k\langle n_H n_P \rangle, \\ \frac{d\langle n_H^2 \rangle}{dt} &= 2k\langle n_H^2 n_P \rangle + k\langle n_H n_P \rangle, \\ \frac{d\langle n_H n_P \rangle}{dt} &= -k\langle n_H^2 n_P \rangle + k\langle n_H n_P^2 \rangle - k\langle n_H n_P \rangle,\end{aligned}\tag{C10}$$

and for $X \notin \{H, P\}$

$$\begin{aligned}\frac{d\langle n_X n_P \rangle}{dt} &= -k\langle n_X n_H n_P \rangle, \\ \frac{d\langle n_X n_H \rangle}{dt} &= k\langle n_X n_H n_P \rangle,\end{aligned}\tag{C11}$$

which are derived from the CME. These equations form the time evolution of the observables under this reaction $d\phi^{(H+P \rightarrow 2H)}/dt$. In the derivation of the desired approximations, the reaction rates are set to unity $k = 1$. Ultimately, if a linear model is learned instead of a neural network, the learned coefficients can be interpreted as the learned reaction rates.

These equations are not closed - higher order observables appear on the right hand side. In principle, any moment closure approximation can be used to derive an approximation, but the natural choice is to use Gaussian moment closure (Equation (3) of the main text) since the model is Gaussian. The space of candidates can also be increased by deriving approximations for more than one closure approximation. Under this approximation, for any species X, Y, Z :

$$\langle n_X n_Y n_Z \rangle \rightarrow -2\langle n_X \rangle \langle n_Y \rangle \langle n_Z \rangle + \langle n_X \rangle \langle n_Y n_Z \rangle + \langle n_Y \rangle \langle n_X n_Z \rangle + \langle n_Z \rangle \langle n_X n_Y \rangle.\tag{C12}$$

This approximation gives the closed form for the observables $d\phi^{(H+P \rightarrow 2H, \text{closed})}/dt$.

To convert back to the parameter frame, we note that the transformation $d\phi/dt \rightarrow d\theta/dt$ may not exist. Instead, we track only a certain number of observables equivalent to the number of parameters D in the model. While the choice of the observables is arbitrary, the obvious choice is those that match the dimensions of the parameters:

$$\frac{d}{dt} \{ \boldsymbol{\mu}_v, C_{vh}, \text{Tr}(C_v), \boldsymbol{\mu}_h, \Sigma_h \},\tag{C13}$$

which match the dimensions of $\boldsymbol{\theta}(t) = \{ \mathbf{b}, W, \sigma^2, \boldsymbol{\mu}_h, \Sigma_h \}(t)$. The transformations are obtained by differentiating Equation (10) of the main text:

$$\begin{aligned}\frac{dW^\top}{dt} &= -\Sigma_h^{-1} \frac{d\Sigma_h}{dt} \Sigma_h^{-1} C_{vh} + \Sigma_h^{-1} \frac{dC_{vh}}{dt}, \\ \frac{d\mathbf{b}}{dt} &= \frac{d\boldsymbol{\mu}_v}{dt} - \frac{dC_{vh}^\top}{dt} \Sigma_h^{-1} \boldsymbol{\mu}_h + C_{vh}^\top \Sigma_h^{-1} \frac{d\Sigma_h}{dt} \Sigma_h^{-1} \boldsymbol{\mu}_h - C_{vh}^\top \Sigma_h^{-1} \frac{d\boldsymbol{\mu}_h}{dt}, \\ \frac{d\sigma^2}{dt} &= \frac{d\text{Tr}(C_v)}{dt} - \text{Tr} \left(\left(\frac{dC_{vh}}{dt} \right)^\top \Sigma_h^{-1} \Sigma_{vh} + C_{vh}^\top \Sigma_h^{-1} \frac{dC_{vh}}{dt} - C_{vh}^\top \Sigma_h^{-1} \frac{d\Sigma_h}{dt} \Sigma_h^{-1} C_{vh} \right).\end{aligned}\tag{C14}$$

The resulting time evolution vector $\mathbf{F}_{H+P \rightarrow 2H}^{(\text{approx.})}(\boldsymbol{\theta}(t))$ is an approximation to the true time evolution. It has been shown that the linearity of the CME in reaction operators extends this form of the approximation [12]. If a linear combination of such approximations is used instead of a neural network, the learned coefficients are directly the reaction rates associated with each process.

Finally, the differential equations can be transformed to the standard parameter space using the inverse of Equation (10) of the main text and its derivative:

$$\begin{aligned}\hat{\mathbf{b}} &= \mathbf{b} + W\boldsymbol{\mu}_h, \\ \hat{W} &= W\Sigma_h^{1/2},\end{aligned}\tag{C15}$$

and

$$\begin{aligned}\hat{F}_{\mathbf{b}} &= F_{\mathbf{b}} + F_W \boldsymbol{\mu}_h + W F_{\boldsymbol{\mu}_h}, \\ \hat{F}_{\hat{W}} &= F_W \Sigma_h^{1/2} + \frac{1}{2} W \Sigma_h^{-1/2} F_{\Sigma_h},\end{aligned}\tag{C16}$$

where (C16) only holds for diagonal latent covariance matrices Σ_h as parameterized in Equation (13) of the main text due to the derivative of the matrix square root. In general, the derivative of the matrix square root may be expressed through a Kronecker sum as $d\Sigma_h^{1/2}/dt = (\Sigma_h^{1/2} \oplus \Sigma_h^{1/2})^{-1}$.

The result of the transformation is $\hat{\mathbf{F}}_{H+P \rightarrow 2H}^{(\text{approx.})}$, the approximation to the time evolution in the standard space.

4. Size of computer algebra expressions

To calculate the reaction approximations, a computer algebra system (Mathematica) was used to derive the expressions. To estimate the size of the analytic expressions, we calculate the number of nodes in the abstract syntax tree for the different reactions considered in Figure 11(b), after using Mathematica to simplify the expressions. The total number of nodes across all reactions for the calculation $\boldsymbol{\theta} \rightarrow \mathbf{F}_{\text{reaction}}^{(\text{approx.})}$ is 1442 nodes. The average number of nodes per reaction is 120. Figure 12 visualizes the syntax tree for all reactions by reaction and by PCA parameter. This measure of the functional forms \mathbf{F} quantifies the amount of domain-specific knowledge brought into the method by the reaction-based model, beyond what's in the parameter-based model.

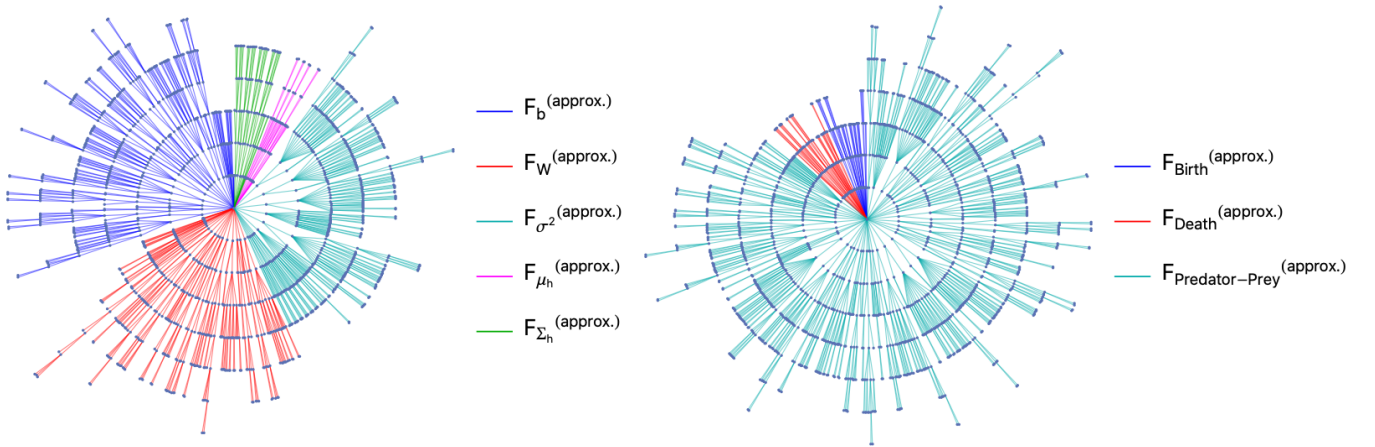


FIG. 12. Visualization of the syntax tree for the reaction approximations of Figure 11(b). Each edge originating from the center node is an individual reaction approximation. *Left*: arranged by PCA parameter $\boldsymbol{\theta}$. *Right*: arranged by reaction type.

5. Standardizing inputs / outputs of subnet

The inputs to the subnet of Figure 1 of the main text are standardized as is typical for neural networks, as well as the target outputs. From the training data $X(t)$ of size M samples by N_v visible variables, the matrix is transformed $X(t) \rightarrow Y(t)$ as discussed previously, and then the standard ML parameters $\hat{\boldsymbol{\theta}}_{\text{ML}}(t)$ are obtained.

The standardization for the outputs is straightforward. By differentiating $\hat{\boldsymbol{\theta}}(t)$ with total variation regularization, the target outputs of the subnet $d\hat{\boldsymbol{\theta}}_{\text{ML}}/dt$ are obtained. The mean and standard deviation are calculated:

$$\begin{aligned}\boldsymbol{\mu}^{(\text{targets})} &= \frac{1}{T} \sum_{t=1}^T \frac{d\hat{\boldsymbol{\theta}}_{\text{ML}}(t)}{dt}, \\ \boldsymbol{\sigma}^{(\text{targets})} &= \left(\frac{1}{T} \sum_{t=1}^T \left(\frac{d\hat{\boldsymbol{\theta}}_{\text{ML}}(t)}{dt} - \boldsymbol{\mu}^{(\text{targets})} \right)^2 \right)^{1/2},\end{aligned}\tag{C17}$$

and the targets are standardized:

$$\frac{d\hat{\boldsymbol{\theta}}_{\text{ML}}(t)}{dt} \rightarrow \left(\frac{d\hat{\boldsymbol{\theta}}_{\text{ML}}(t)}{dt} - \boldsymbol{\mu}^{(\text{targets})} \right) / \boldsymbol{\sigma}^{(\text{targets})}. \quad (\text{C18})$$

Standardizing the inputs is not straightforward because they depend on the latent parameters $\boldsymbol{\mu}_h, \Sigma_h$, which are defined by their Fourier coefficients (Equation (13) of the main text), which are learned. The standardizing parameters may be learned with a normalizing layer, but this is challenging in practice. Instead, we bootstrap the inputs to estimate these parameters as follows. Keep only the highest frequency f_{max} in the Fourier expansion (Equation (13) of the main text), and set all corresponding coefficients $a = b = 1$. Then the ML parameters are bootstrapped with this choice for $\boldsymbol{\mu}_h, \Sigma_h$ to estimate the inputs $\hat{\mathbf{F}}_{A+B \rightarrow 2B}^{(\text{approx.})}$ for the different reactions, and the standardization proceeds for each reaction in the usual way:

$$\begin{aligned} \boldsymbol{\mu}_{A+B \rightarrow 2B}^{(\text{inputs})} &= \frac{1}{T} \sum_{t=1}^T \hat{\mathbf{F}}_{A+B \rightarrow 2B}^{(\text{approx.})}(\hat{\boldsymbol{\theta}}(t)), \\ \boldsymbol{\sigma}_{A+B \rightarrow 2B}^{(\text{inputs})} &= \left(\frac{1}{T} \sum_{t=1}^T \left(\hat{\mathbf{F}}_{A+B \rightarrow 2B}^{(\text{approx.})}(\hat{\boldsymbol{\theta}}(t)) - \boldsymbol{\mu}_{A+B \rightarrow 2B}^{(\text{inputs})} \right)^2 \right)^{1/2}, \\ \hat{\mathbf{F}}_{A+B \rightarrow 2B}^{(\text{approx.})} &\rightarrow \left(\hat{\mathbf{F}}_{A+B \rightarrow 2B}^{(\text{approx.})} - \boldsymbol{\mu}_{A+B \rightarrow 2B}^{(\text{inputs})} \right) / \boldsymbol{\sigma}_{A+B \rightarrow 2B}^{(\text{inputs})}. \end{aligned} \quad (\text{C19})$$

Appendix D: Learned model of Calcium oscillations

1. Frequencies

The latent mean and variance are learned in parallel to the parameters in the differential equation model. By not fixing these parameters, the model is more easily able to find a non-intersecting trajectory in θ -space. The latent parameters μ_h, Σ_h are represented by the Fourier decomposition given in Equation (13) of the main text.

Figure 13 shows the frequencies chosen for calcium oscillation models (Figure 3 of the main text and Figure 4 of the main text). The frequencies $f_n = \{1, 2, 3, 4, 5, 6\} \times 2\pi/40 \text{ s}^{-1}$ allow oscillations on the same period as the calcium oscillations over several seconds.

2. Learned latent representation

Figure 14 shows the learned latent mean μ_h in this representation for the four models of Figure 3 of the main text: a deep & wide subnet compared to a shallow & thin subnet, with each a reaction-based model compared to parameter-only model without reactions. The learned frequencies for the reaction-based model are more coherent than for the parameter-only model as seen in Figure 14, and similarly for Σ_h . This coherence suggests that the network uncovers an emergent order parameter.

3. Learned moment closure approximation

DBDs learn a moment closure approximation from data. The reduced model evolves in time as:

$$\frac{d\tilde{p}}{dt} = \sum_{\theta \in \theta} \frac{\partial \tilde{p}}{\partial \theta} \times F_{\theta}, \quad (\text{D1})$$

where $F_{\theta}(\theta) = d\theta/dt$ by definition. An observable $\langle X(\mathbf{n}) \rangle$ where $X(\mathbf{n})$ is some scalar function evolves according to:

$$\frac{d\langle X(\mathbf{n}) \rangle}{dt} = \sum_{\theta \in \theta} \left(\sum_{\mathbf{n}} X(\mathbf{n}) \frac{\partial \tilde{p}}{\partial \theta} \right) \times F_{\theta}. \quad (\text{D2})$$

For maximum-entropy distributions, this quantity is a covariance between $X(\mathbf{n})$ and the moments controlled by interactions in the energy function [14]. For example, for a restricted Boltzmann machine, correlations between visible units have been replaced by correlations with latent variables, whose activation is learned. For the Gaussian distribution of PCA, it is easiest to work out the equations numerically.

Figure 15 plots the terms for the mean number of calcium $X(\mathbf{n}) = n_{\text{Ca}}$ in the models corresponding to Figure 3 of the manuscript. The terms show that the F_{μ_h} term is learned to be a counter-phase variable to the $F_{b_{\text{Ca}}}$ term. The oscillations for the reaction-based model are more coherent, have higher amplitude and frequency on the order of the calcium oscillations. On the other hand, the parameter-based model oscillates at a higher frequency and lower amplitude. This shows that in the comparison model, the inaccuracies in the learned parameters result partially from finding a flawed latent representation in μ_h and Σ_h .

4. Comparison model without reaction approximations

Figure 16 shows the architecture of the comparison model to Figure 1 of the main text. The network architecture is equivalent except that the reaction approximations are missing. Therefore, the network must learn the functional forms from scratch from the parameters $\theta(t)$.

5. Mean-squared error (MSE)

The mean-squared error (MSE) over parameters in learned models is shown in Figure 4 of the main text. Let $\hat{\theta}_{\text{int}}(t; [\text{IP}_3])$ be the integrated parameters after learning the reduced model for a single IP_3 concentration, and

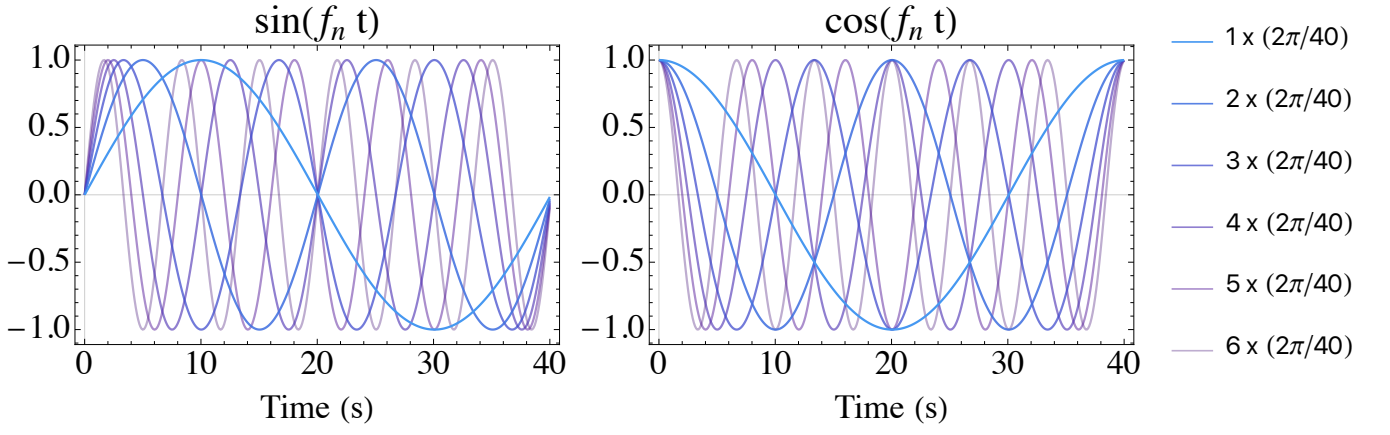


FIG. 13. Frequencies in Equation (13) of the main text used to train the DBD models. The frequencies are chosen to represent oscillations on the same order of magnitude as the calcium oscillations over several seconds.

$\hat{\theta}_{\text{ML}}(t; [\text{IP}_3])$ the maximum likelihood parameters identified from the data. The MSE at a single IP_3 concentration is then given by:

$$\text{MSE}([\text{IP}_3]) = \frac{1}{T} \sum_{t=1}^T |\hat{\theta}_{\text{int}}(t; [\text{IP}_3]) - \hat{\theta}_{\text{ML}}(t; [\text{IP}_3])|^2. \quad (\text{D3})$$

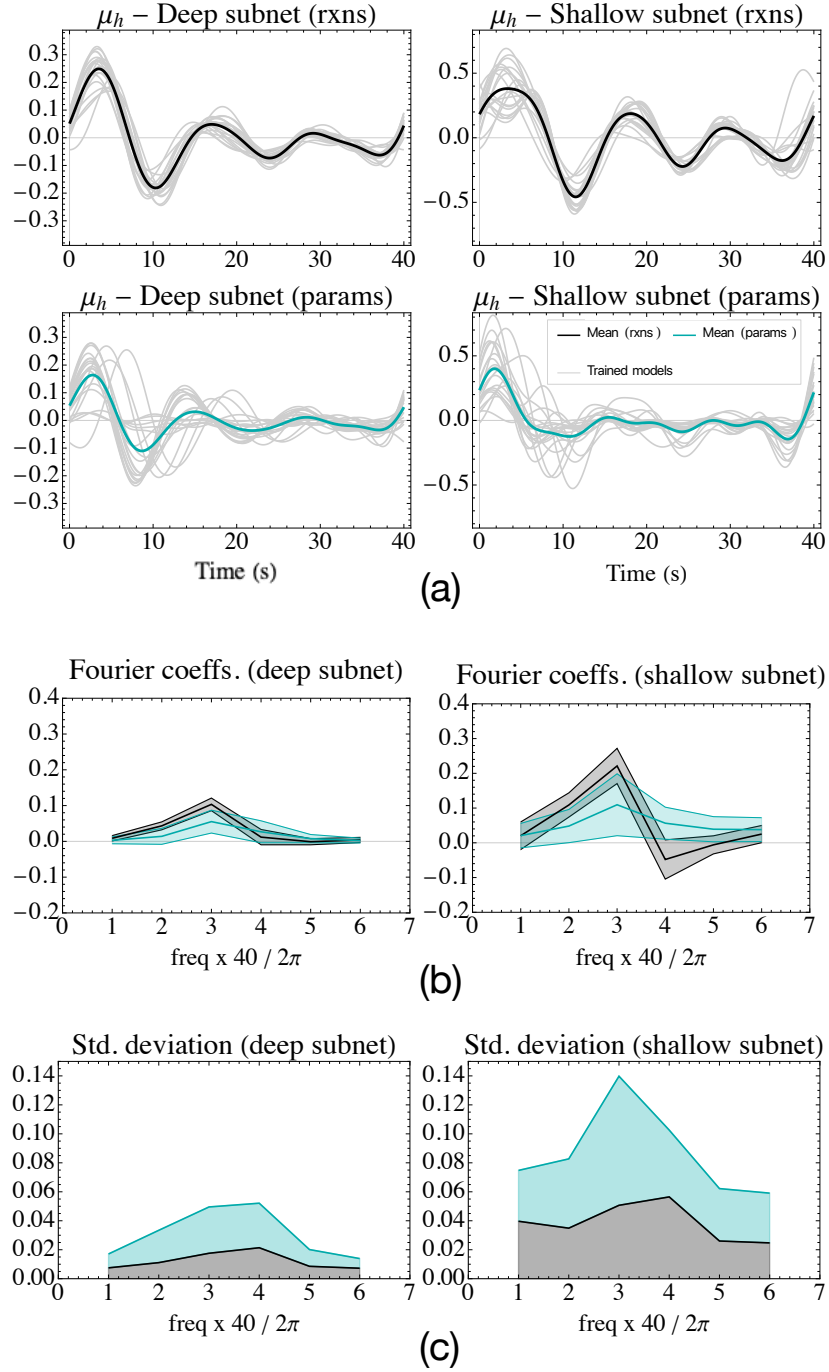


FIG. 14. (a) Learned μ_h time evolution according to the Fourier representation (Equation (13) of the main text) for 20 identical trained models and their mean. *Left column*: deep & wide subnet as shown in Figure 3 of the main text; *bottom row*: shallow & thin subnet. *Right column*: reactions based model as shown in Figure 1 of the main text; *right column*: comparison model without reaction approximations as shown in Figure 16. (b) The learned Fourier coefficients for μ_h . (c) The standard deviation of the coefficients. The coefficients in the reaction based model are more coherent.

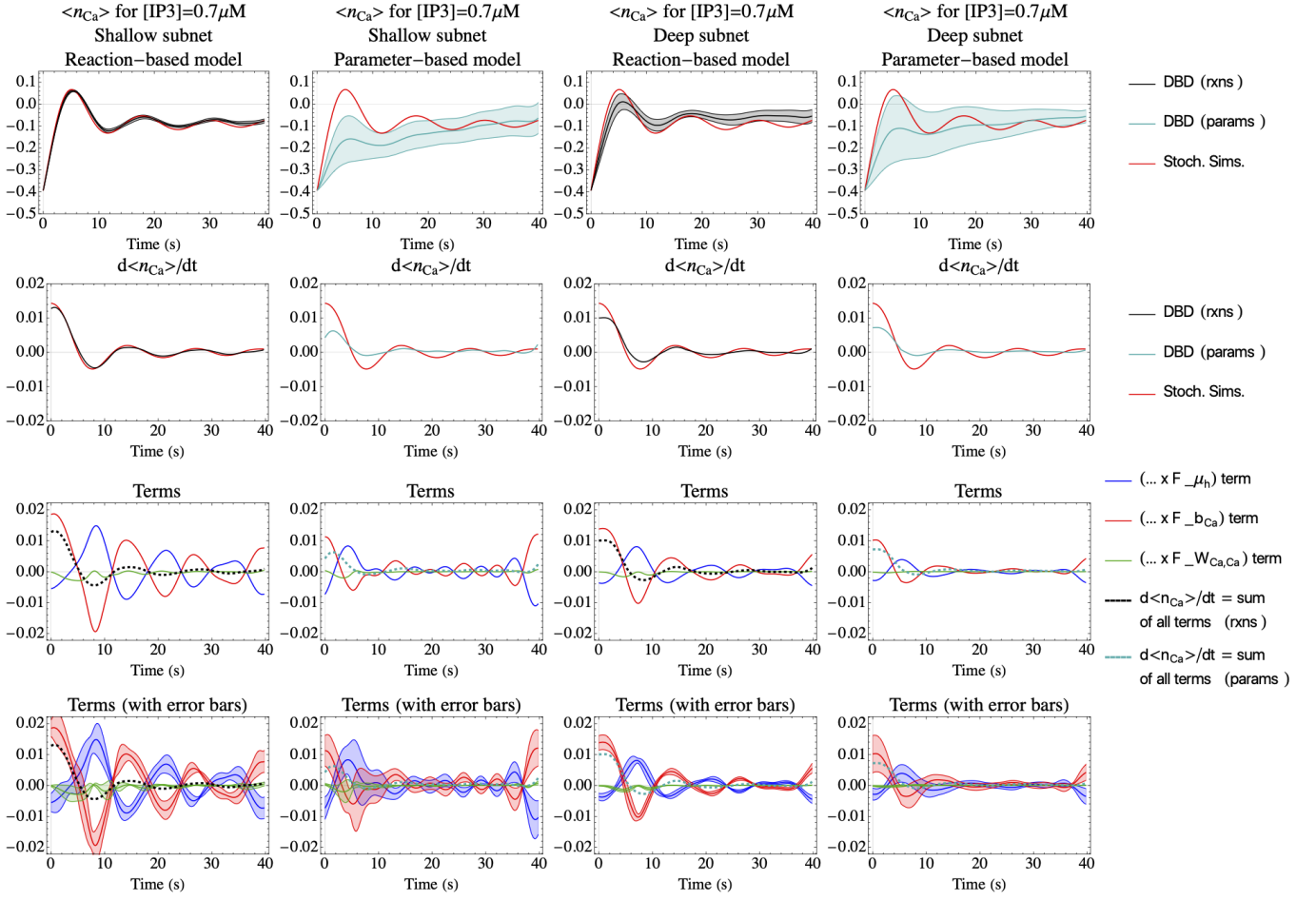


FIG. 15. Moment closure terms learned corresponding to the model of Figure 3 of the manuscript. *First column*: the shallow subnet model for the reaction-based framework. *Second column*: shallow subnet, parameter model. *Third column*: deep subnet, reaction model. *Fourth column*: deep subnet, parameter model. *First row*: At a single concentration of $IP_3 = 0.7\mu M$, the mean number of calcium $\langle n_{Ca} \rangle$ is shown for DBD models, with ground truth from the stochastic simulations in red. *Second row*: The derivative in time of the mean calcium concentration: $d\langle n_{Ca} \rangle/dt$. *Third row*: The terms in Equation (3) for the mean calcium $X(\mathbf{n}) = n_{Ca}$. *Fourth row*: Same as third row with error bars from 10 optimization trials.

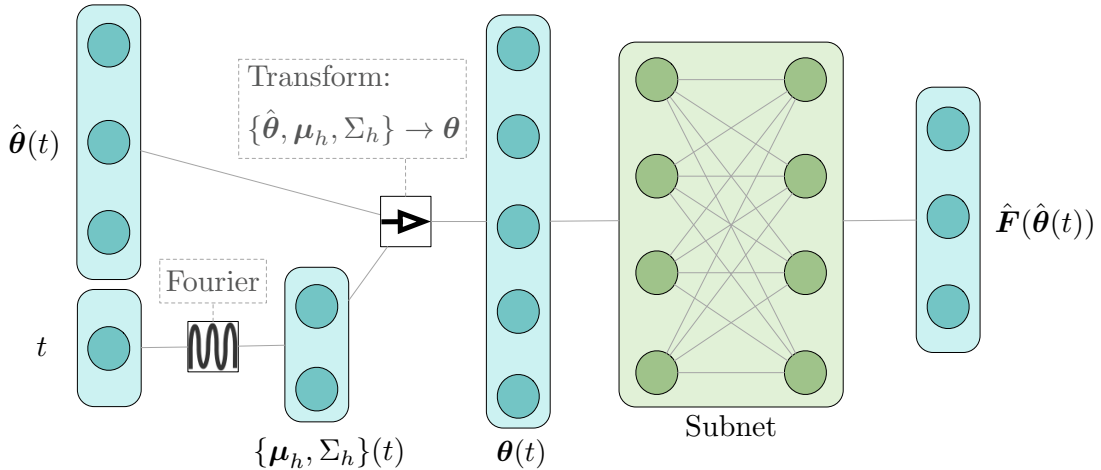


FIG. 16. Comparison architecture similar to Figure 1 of the main text, but missing the analytically derived reaction approximations. Instead, the inputs to the subnet model are the interaction parameters directly.